LETTER

doi:10.1038/nature17411

Detection of a Cooper-pair density wave in $Bi_2Sr_2CaCu_2O_{8+x}$

M. H. Hamidian[1]*, S. D. Edkins[2,3]*, Sang Hyun Joo[4,5]*, A. Kostin[2], H. Eisaki[6], S. Uchida[6,7], M. J. Lawler[2,8], E.-A. Kim[2], A. P. Mackenzie[3,9], K. Fujita[10], Jinho Lee[4,5] & J. C. Séamus Davis[2,3,10,11]

The quantum condensate of Cooper pairs forming a superconductor was originally conceived as being translationally invariant. In theory, however, pairs can exist with finite momentum Q, thus generating a state with a spatially modulated Cooper-pair density[1,2]. Such a state has been created in ultracold ^{6}Li gas[3] but never observed directly in any superconductor. It is now widely hypothesized that the pseudogap phase[4] of the copper oxide superconductors contains such a 'pair density wave' state[5–21]. Here we report the use of nanometre-resolution scanned Josephson tunnelling microscopy[22–24] to image Cooper pair tunnelling from a *d*-wave superconducting microscope tip to the condensate of the superconductor $Bi_2Sr_2CaCu_2O_{8+x}$. We demonstrate condensate visualization capabilities directly by using the Cooper-pair density variations surrounding zinc impurity atoms[25] and at the $Bi_2Sr_2CaCu_2O_{8+x}$ crystal supermodulation[26]. Then, by using Fourier analysis of scanned Josephson tunnelling images, we discover the direct signature of a Cooper-pair density modulation at wavevectors $Q_P \approx (0.25, 0)2\pi/a_0$ and $(0, 0.25)2\pi/a_0$ in $Bi_2Sr_2CaCu_2O_{8+x}$. The amplitude of these modulations is about five per cent of the background condensate density and their form factor exhibits primarily *s* or *s′* symmetry. This phenomenology is consistent with Ginzburg–Landau theory[5,13,14] when a charge density wave[5,27] with *d*-symmetry form factor[28–30] and wavevector $Q_C = Q_P$ coexists with a *d*-symmetry superconductor; it is also predicted by several contemporary microscopic theories for the pseudogap phase[18–21].

When hole doping suppresses the cuprate antiferromagnetic insulator state the pseudogap regime emerges[4]. Both the high-temperature superconducting state and a charge density wave (CDW) state[27] exist therein. However, a 'pair density wave' (PDW) state, in which the Cooper-pair density modulates spatially at wavevector $\boldsymbol{Q}$, is also widely hypothesized[5–21] to exist in the pseudogap regime. There are compelling theoretical motivations for a cuprate PDW state. First, microscopic theories for local electronic structure of the hole-doped antiferromagnet predict a cuprate PDW state linked to combined modulations of hole density and antiferromagnetic spin density[6–10]. Second, *c*-axis superconductivity does not appear in $La_{2-x}Ba_xCuO_4$ until temperatures far below the point at which the CuO_2 planes superconduct, a situation that could be explained by the existence of an orthogonal PDW state in each CuO_2 plane[5,11,13]. Third, the existence of a PDW

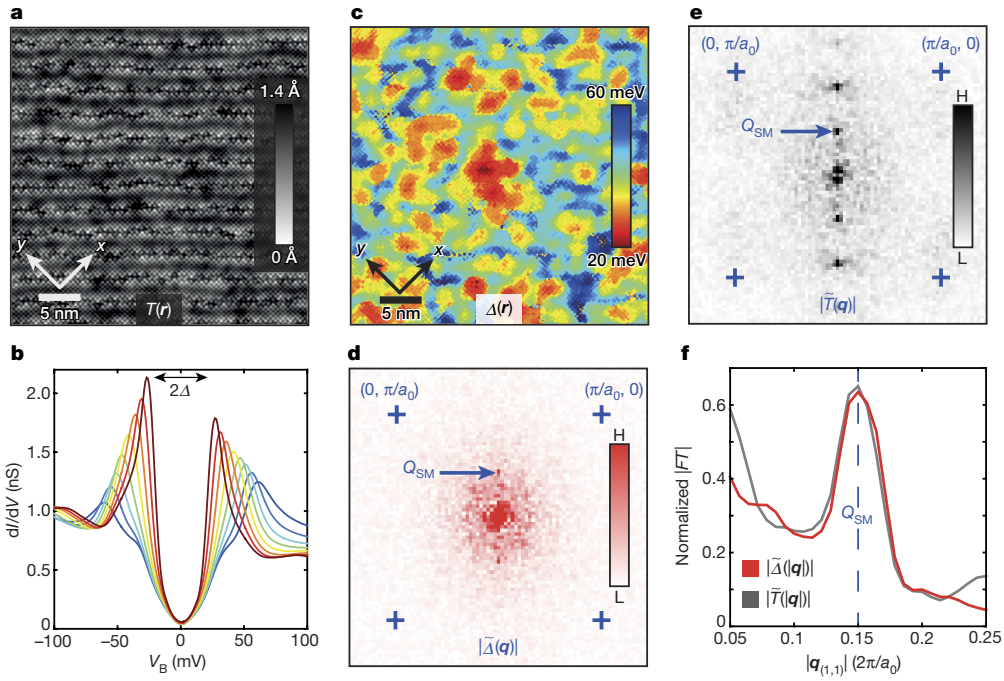

Figure 1 | Spatial variations and modulations in cuprate energy gaps. **a**, Typical 35 nm × 35 nm topographic image $T(\boldsymbol{r})$ of the $Bi_2Sr_2CaCu_2O_{8+x}$ surface (crystal 'supermodulation' runs vertically). **b**, Typical differential conductance spectra of $Bi_2Sr_2CaCu_2O_{8+x}$. The maximum energy gap Δ is half the distance between peaks. V_B is the bias voltage. **c**, Spatial arrangement of $\Delta(\boldsymbol{r})$ (the gapmap) for $p \approx 17\%$ $Bi_2Sr_2CaCu_2O_{8+x}$ in the same field of view as **a**. **d**, The magnitude of the Fourier transform of **c**, $|\widetilde{\Delta}(\boldsymbol{q})|$ (blue crosses are at $\boldsymbol{q} = (\pi/a_0, 0); (0, \pi/a_0)$), showing a single peak due to the supermodulation[26] (blue arrow). H, high; L, low. **e**, The magnitude of the Fourier transform of topograph $|\widetilde{T}(\boldsymbol{q})|$ (blue crosses are at $\boldsymbol{q} = (\pi/a_0, 0); (0, \pi/a_0)$). The supermodulation is a quasi-periodic modulation along the (1,1) direction with wavevector $\boldsymbol{Q}_{SM}$ indicated by the blue arrow. **f**, Simultaneously measured $\widetilde{\Delta}(\boldsymbol{q})$ and $\widetilde{T}(\boldsymbol{q})$ from **d** and **e** along the (1,1) direction. Their primary peaks coincide. FT, Fourier transform; normalization is to DC component.

[1]Department of Physics, Harvard University, Cambridge, Massachusetts 02138, USA. [2]Laboratory of Atomic and Solid State Physics, Department of Physics, Cornell University, Ithaca, New York 14853, USA. [3]School of Physics and Astronomy, University of St Andrews, Fife KY16 9SS, UK. [4]Institute of Applied Physics, Department of Physics and Astronomy, Seoul National University, Seoul 151-747, South Korea. [5]Center for Correlated Electron Systems, Institute of Basic Science, Seoul 151-742, South Korea. [6]Institute of Advanced Industrial Science and Technology, Tsukuba, Ibaraki 305-8568, Japan. [7]Department of Physics, University of Tokyo, Bunkyo, Tokyo 113-0011, Japan. [8]Department of Physics, Binghamton University, Binghamton, New York 13902-6000, USA. [9]Max Planck Institute for Chemical Physics of Solids, D-01187 Dresden, Germany. [10]Condensed Matter Physics and Materials Science Department, Brookhaven National Laboratory, Upton, New York 11973, USA. [11]Kavli Institute at Cornell for Nanoscale Science, Cornell University, Ithaca, New York 14853, USA.
*These authors contributed equally to this work.

© 2016 Macmillan Publishers Limited. All rights reserved

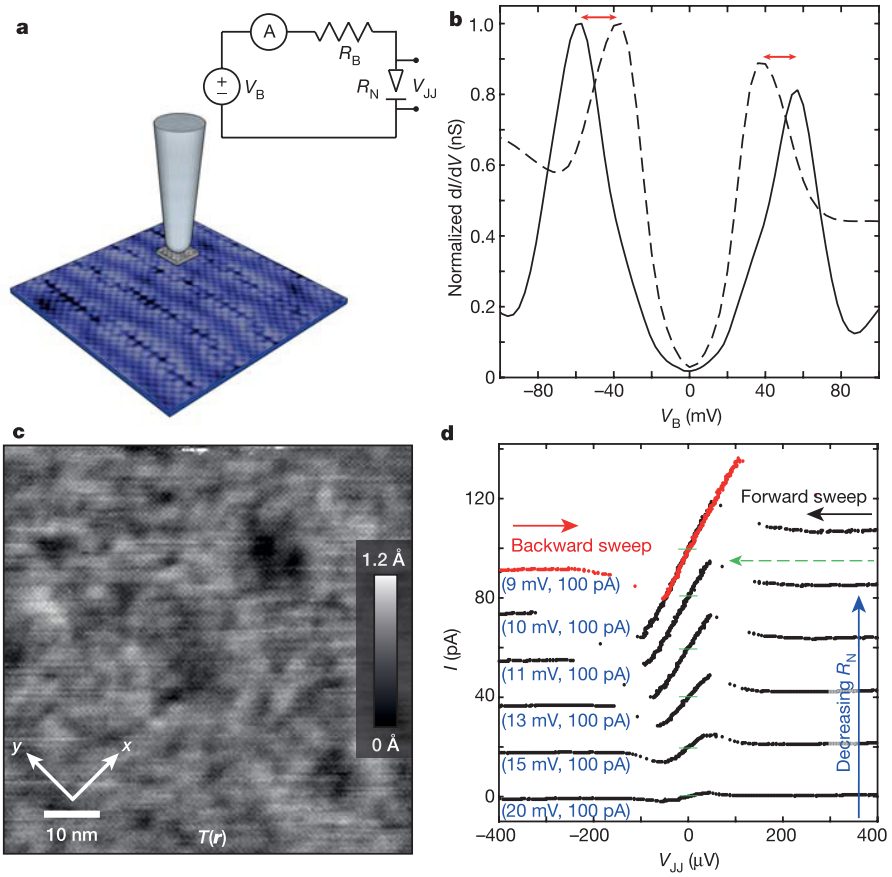

Figure 2 | *d*-wave HTS tip fabrication for SJTM. a, Schematic STM tip with nanometre-sized $Bi_2Sr_2CaCu_2O_{8+x}$ flake adhering. Inset, combined spectroscopic-imaging STM and Josephson circuitry used ($R_B = 10\,M\Omega$). **b**, Conversion of single-particle NIS (dashed) to single-particle SIS (solid) spectra when $Bi_2Sr_2CaCu_2O_{8+x}$ nano-flake adheres to tungsten tip. The tip gap $\Delta_T \approx 25$ meV is the difference between the NIS and SIS peaks (red double-headed arrows). **c**, Topographic image $T(\boldsymbol{r})$ (76 nm × 76 nm) using single-particle SIS tunnelling with the same tip as in **a** and **b**. Spatial resolution is ~1 nm. Absence of moiré patterns in its Fourier transform (see Methods section 'Characterizing $Bi_2Sr_2CaCu_2O_{8+x}$ nano-flake STM tips') indicates that the nanoflake's crystal axes (superconducting order parameter) are aligned with the bulk crystal axes (superconducting order parameter). **d**, Measured evolution of the SJTM $I(V)$ with diminishing tip–sample distance (diminishing R_N) at $T = 45$ mK (junction formation conditions given in blue text). The maximum current I_c for a typical $I(V)$ is indicated by a dashed green arrow.

state could explain some of the unusual characteristics observed in the single-particle excitations[15–17]. Finally, contemporary theories for the cuprate pseudogap phase hypothesize a composite state in which the CDW is directly linked to a PDW of the same wavevector[18–21].

The definitive signature[1,2,5] of a PDW would be a periodic modulation of the Cooper-pair condensate density with wavevector $\boldsymbol{Q}$. In principle, this could be visualized using two techniques. First, scanning tunnelling microscopy (STM) using conventional single-electron tunnelling may detect modulations at $\boldsymbol{Q}$ in the locally defined energy gap:

$$\Delta(\boldsymbol{r}) = \Delta_0 + \Delta_P \cos(\boldsymbol{Q}\cdot\boldsymbol{r}) \quad (1)$$

Here Δ_0 is the homogeneous superconductor energy gap and $\Delta_P\cos(\boldsymbol{Q}\cdot\boldsymbol{r})$ is that of the PDW (refs 1 and 2). A second possibility is scanned Josephson tunnelling microscopy (SJTM) of Cooper pairs[22–24] to detect the modulations of Cooper-pair density directly. Again, in the presence of the homogeneous condensate, this should result in a modulating Josephson critical current I_J:

$$I_J(\boldsymbol{r}) = I_J^0 + I_J^P \cos(\boldsymbol{Q}\cdot\boldsymbol{r}) \quad (2)$$

where the first term represents Cooper-pair tunnelling to a homogeneous condensate and the second to the PDW. Imaging the spatial arrangements of the superfluid density $\rho_S(\boldsymbol{r})$ would then be possible, since $I_J^2(\boldsymbol{r}) \propto \rho_S(\boldsymbol{r})$ (see Methods section 'Modelling phase diffusion Josephson dynamics for SJTM').

The phenomena in equation (1) have not been detected in a cuprate (or any other) superconductor. One challenge is the extreme variation in the differential tunnelling conductance spectra (Fig. 1b) typically detected at the $Bi_2Sr_2CaCu_2O_{8+x}$ surface $T(\boldsymbol{r})$ (Fig. 1a). Visualizing the maximum energy gap (double-headed black arrow in Fig. 1b) yields a heterogeneous 'gapmap' $\Delta(\boldsymbol{r})$ (Fig. 1c), whose Fourier transform $\widetilde{\Delta}(\boldsymbol{q})$ (Fig. 1d) exhibits only one sharp finite-$\boldsymbol{q}$ peak (blue arrow). This $\Delta(\boldsymbol{r})$ modulation occurs at the wavevector $\boldsymbol{Q}_{SM}$ of a quasi-periodic distortion of the $Bi_2Sr_2CaCu_2O_{8+x}$ crystal unit cell along the CuO_2 (1,1) direction[26] that is referred to as the 'supermodulation' (Fig. 1e). Because no other periodic modulations of the maximum energy gap Δ (or any other energy gap) have been detected in cuprate gapmap studies, searches for a cuprate PDW via equation (1) yield a null result.

The use of superconducting STM tips to measure the spatial variation of Cooper-pair tunnelling (SJTM) therefore remains the most promising approach with which to search for a PDW state (equation (2)). For two superconducting electrodes with temperature dependent energy gaps $\Delta(T)$ and phases ϕ_1 and ϕ_2, the Josephson current is given by $I(\phi) = I_J\sin(\phi)$ where $\phi = \phi_2 - \phi_1$. The Josephson critical current I_J is given by $I_J R_N = \frac{\pi\Delta(T)}{2e}\tanh(\Delta(T)/2kT)$ where R_N is the normal-state junction resistance, k is the Boltzmann constant, and $2e$ is the Cooper-pair charge. Time independence of ϕ would require the Josephson energy $E_J = \frac{\phi_0 I_J}{2\pi}$, where ϕ_0 is the magnetic flux quantum, to exceed the thermal fluctuation energy kT. For a nanometre-sized Josephson junction with sub-nanoampere I_J, this regime remains out of reach at

© 2016 Macmillan Publishers Limited. All rights reserved

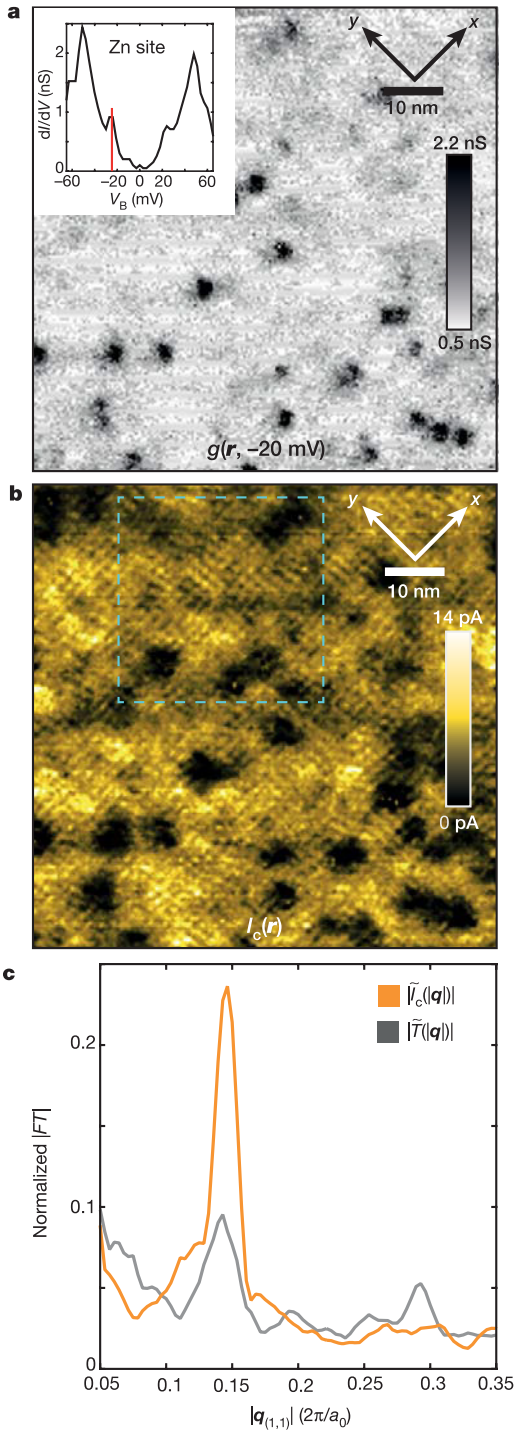

Figure 3 | Cooper-pair condensate visualization using SJTM. a, The convolution of $\Omega = -1.5$ meV Zn impurity resonance with the *d*-wave spectrum of the tip shifts the resonance to $|E| \approx |\Omega| + |\Delta_T|$. The measured SIS $g(\boldsymbol{r}, E = -20\,\text{meV})$ 76 nm × 76 nm image near this energy (vertical red line) identifies the site of each Zn. **b**, A 76 nm × 76 nm $I_c(\boldsymbol{r})$ image measured at 45 mK in the same field of view as **a**. A deep minimum (~95% suppression) occurs in $I_c(\boldsymbol{r})$ surrounding each Zn site where the Cooper-pair condensate is suppressed[25]. **c**, Simultaneously measured magnitude of $\tilde{I}_c(\boldsymbol{q})$ and $\tilde{T}(\boldsymbol{q})$ along the CuO_2 (1,1) direction. The primary peaks in $\tilde{I}_c(\boldsymbol{q})$ and from the supermodulation coincide, demonstrating the ability to visualize Cooper-pair density modulations.

millikelvin temperatures. However, imaging of phase-diffusion-dominated Josephson tunnelling is possible by using superconducting-tip STM to measure an $I(V)$ whose maximum current is $I_c \propto I_J^2$ (refs 22–24 and Methods section 'Modelling phase diffusion Josephson dynamics for SJTM').

To search for a cuprate PDW near $\boldsymbol{Q} \approx (0.25, 0)2\pi/a_0$ and $(0, 0.25)2\pi/a_0$ where $a_0 \approx 3.8$ Å also requires visualizing $I_c(\boldsymbol{r}) \propto I_J^2(\boldsymbol{r})$ with nanometre resolution. Moreover, high Δ, low R_N and millikelvin operating temperatures would all be highly advantageous. Motivated in this way, we use a dilution-refrigerator-based STM operated below 50 mK, and achieve a high tip-energy gap Δ_T by picking up a nanometre-sized flake of $Bi_2Sr_2CaCu_2O_{8+x}$ on the end of our tungsten tip (see Fig. 2a and Methods section 'Characterizing $Bi_2Sr_2CaCuO_{8+x}$ nano-flake STM tips'). This immediately converts our measured normal–insulator–superconductor (NIS) tunnelling spectrum (dashed line in Fig. 2b) to a superconductor–insulator–superconductor (SIS) spectrum (solid line in Fig. 2b) exhibiting an energy separation of about $2(\Delta_S + \Delta_T)$ between conductance peaks (Methods section 'Characterizing $Bi_2Sr_2CaCuO_{8+x}$ nano-flake STM tips'). Figure 2b demonstrates that our *d*-wave high-temperature superconducting (HTS) tip has $\Delta_T \approx 25$ meV (double-headed red arrows), and its spatial resolution is evaluated to be 1 nm using a topographic image of the BiO surface of $Bi_2Sr_2CaCu_2O_{8+x}$ (Fig. 2c) that was measured using this tip in the single-particle tunnelling regime (Methods section 'Characterizing $Bi_2Sr_2CaCuO_{8+x}$ nanoflake STM tips'). Next, we measure the $I(V)$ characteristic of this tip as a function of decreasing tip distance from the bulk crystal surface, and thus of decreasing R_N. At $T = 45$ mK and fixed $\boldsymbol{r}$, as the superconducting tip is moved forward in ~10-picometre steps the evolution of $I(V)$ characteristics is as shown in Fig. 2d. As the Josephson I_J increases with diminishing distance, the maximum observable current $I_c \propto I_J^2$ increases as expected (see Methods section 'Modelling phase diffusion Josephson dynamics for SJTM' and 'Characterizing $Bi_2Sr_2CaCuO_{8+x}$ nanoflake STM tips').

To test the Cooper-pair condensate visualization capabilities of this $I_c(\boldsymbol{r})$ imaging technique directly, we use two approaches. First, when Zn impurity atoms are substituted at the Cu sites, muon spin rotation studies show that the Cooper-pair condensate is completely suppressed in a radius of a few nanometres around each Zn atom, in a "Swiss cheese" configuration[25]. Figure 3a shows a 76 nm × 76 nm image of SIS single-particle tunnelling conductance $g(\boldsymbol{r}, -20\,\text{meV})$ using the same tip. One can locate each Zn impurity atom by its scattering resonance peak, which is shifted by convolution with the superconducting tip spectrum from its resonance energy $\Omega = -1.5$ meV to $|E| \approx |\Omega| + |\Delta_T| \approx 25$ meV (vertical red line in the inset to Fig. 3a). Thus, the Zn impurity atoms are at the dark spots in Fig. 3a. In Fig. 3b we show $I_c(\boldsymbol{r})$ measured at ~50 mK in the same field of view as Fig. 3a. This reveals how $I_c(\boldsymbol{r})$, and thus the Cooper-pair condensate, is suppressed within a radius $R \approx 3$ nm of each Zn atom site, consistent with muon spin rotation studies[25]. A second test is possible because of the crystal 'supermodulation' and the associated modulating superconductivity at wavevector $\boldsymbol{Q}_{SM}$ (ref. 26) (Fig. 1f). In Fig. 3c we plot the magnitude of the Fourier transform $\tilde{T}(\boldsymbol{q})$ in grey and $\tilde{I}_c(\boldsymbol{q})$ in orange, both measured simultaneously along the (1,1) direction through $\boldsymbol{Q}_{SM}$. This directly demonstrates the capability to visualize the Cooper-pair density modulations that are induced by the $Bi_2Sr_2CaCu_2O_{8+x}$ crystal supermodulation. Overall, these tests show that nanometre-resolution Cooper-pair condensate visualization is achievable using this *d*-wave high-gap tip, combined with our millikelvin-operating-temperature SJTM approach.

Next, we apply this technique to search for a cuprate PDW in the same $Bi_2Sr_2CaCu_2O_{8+x}$ samples with $T_c = 88$ K and hole density $p = 17\%$ and at $T < 50$ mK (see Methods section 'Defining, measuring and imaging $I_c(\boldsymbol{r})$'). The two states already reported to coexist at this *p* value are the high-temperature superconductor and a CDW with $\boldsymbol{Q} = (0.22 \pm 0.02, 0)2\pi/a_0$ and $(0, 0.22 \pm 0.02)2\pi/a_0$ (ref. 27). Figure 4a shows our measured $I_c(\boldsymbol{r})$ in the 35 nm × 35 nm field of view (blue dashed box in Fig. 3b). Clear $I_c(\boldsymbol{r})$ modulations are immediately observable and, given that $I_c(\boldsymbol{r}) \propto (I_J^0)^2 + 2I_J^0 I_J^P \cos(\boldsymbol{Q}\cdot\boldsymbol{r}) + (I_J^P)^2 \cos^2(\boldsymbol{Q}\cdot\boldsymbol{r})$

© 2016 Macmillan Publishers Limited. All rights reserved

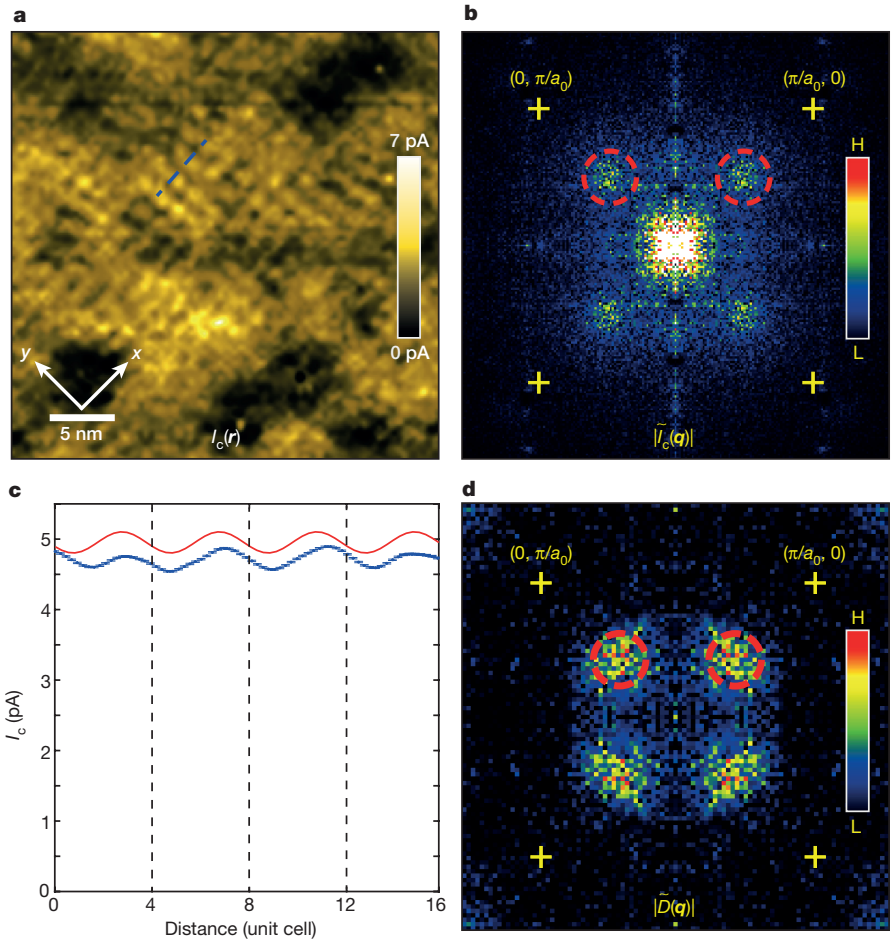

Figure 4 | Visualizing the Cooper-pair density wave in $Bi_2Sr_2CaCu_2O_{8+x}$. **a**, A 35 nm × 35 nm field of view $I_c(\boldsymbol{r})$ image (dashed blue box in Fig. 3b) showing the $I_c(\boldsymbol{r})$ modulations parallel to the CuO_2 x and y axes (supermodulation-induced $I_c(\boldsymbol{r})$ modulations are removed). **b**, $|\widetilde{I_c}(\boldsymbol{q})|$, the Fourier transform of $I_c(\boldsymbol{r})$ in **a** (yellow crosses at $\boldsymbol{q} = (\pi/a_0, 0)$ and $(0, \pi/a_0)$). Maxima from $I_c(\boldsymbol{r})$ modulations (dashed red circles) occur at $\boldsymbol{Q}_P = (0.25, 0)2\pi/a_0$ and $(0, 0.25)2\pi/a_0$, and no significant modulations occur in $\widetilde{R}_N(\boldsymbol{Q}_P)$ (see Methods section 'Visualizing supermodulation-induced PDW and $R_N(\boldsymbol{r})$'). **c**, Measured $I_c(\boldsymbol{r})$ along the dashed blue line in **a** (blue dotted line); statistical error bars are the variance of I_c transverse to the dashed line. The red line shows the global amplitude and $\boldsymbol{Q}_P$ of the $I_c(\boldsymbol{r})$ modulations (from the circled maxima in **b**). **d**, Magnitude of $\widetilde{D}(\boldsymbol{q}) = \widetilde{O}_x(\boldsymbol{q}) - \widetilde{O}_y(\boldsymbol{q})$ (yellow crosses at $\boldsymbol{q} = (\pi/a_0, 0);(0, \pi/a_0)$) revealing the d-symmetry form factor density wave modulations (dashed red circles) at $\boldsymbol{Q}_C = (0.22, 0)2\pi/a_0$; $(0, 0.22)2\pi/a_0$ (same hole density as in **b**).

from equation (2), they provide the magnitude and wavevector of the component $I_J^P(\boldsymbol{r})$ modulations. The magnitude of the Fourier transform of $I_c(\boldsymbol{r})$, $|\widetilde{I_c}(\boldsymbol{q})|$, is shown in Fig. 4b, revealing that modulation in $I_c(\boldsymbol{r})$ occurs at the wavevectors $\boldsymbol{Q}_P = (0.25 \pm 0.02, 0)2\pi/a_0$ and $(0, 0.25 \pm 0.02)2\pi/a_0$ (dashed red circles in Fig. 4b), while nothing is observable in the second harmonic $\cos^2(\boldsymbol{Q} \cdot \boldsymbol{r})$. This situation seems to occur because the $I_J^P(\boldsymbol{r})$ modulations are superposed on a much stronger spatially constant critical current I_J^0 (equation (2)). These data provide strong *a priori* evidence for the existence of a PDW coexisting with a robust Cooper-pair condensate in $Bi_2Sr_2CaCu_2O_{8+x}$. In Fig. 4c we show (as blue dots) the measured value of $I_c(\boldsymbol{r})$ along the blue line in Fig. 4a, while we show the amplitude and wavelength of the global $I_c(\boldsymbol{r})$ modulations (determined from the magnitude and central $\boldsymbol{Q}$ value of the peaks in Fig. 4b) as a red line. From these data, and in general from the magnitude of the peaks at Q_x and Q_y in Fig. 4b, we conclude that the modulation amplitude in Cooper-pair density is ~5% of its average value. Therefore the cuprate PDW at $p = 17\%$ is subdominant to the d-wave superconducting state below 50 mK.

Finally, in Fig. 4d we study $\widetilde{D}(\boldsymbol{q}) = \widetilde{O}_x(\boldsymbol{q}) - \widetilde{O}_y(\boldsymbol{q})$, the oxygen-sublattice-phase-resolved image of d-symmetry form factor density modulations[28–30], from a $Bi_2Sr_2CaCu_2O_{8+x}$ sample with the same hole density (see Methods section 'Imaging d-symmetry CDW $\widetilde{D}(\boldsymbol{q})$ and avoiding the CDW setup effect in $I_c(\boldsymbol{r})$'). The conventional locations of d-symmetry form factor CDW peaks in $\widetilde{D}(\boldsymbol{q})$ (dashed red circles) occur at $\boldsymbol{Q}_C = (0.22 \pm 0.04, 0)2\pi/a_0$ and $(0, 0.22 \pm 0.04)2\pi/a_0$. We note that in the unprocessed data the modulations in electronic structure and topography occur based upon the sum of both oxygen sublattices $(\widetilde{O}_x(\boldsymbol{q}) + \widetilde{O}_y(\boldsymbol{q}))$ and at wavevector $\boldsymbol{Q} = \boldsymbol{Q}_{Bragg} \pm \boldsymbol{Q}_C$ (ref. 28). No response of the tip to these modulations could produce a spurious $I_c(\boldsymbol{r})$ modulation at the PDW wavevector $\boldsymbol{Q}_P = (0.25 \pm 0.02, 0)2\pi/a_0$ and $(0, 0.25 \pm 0.02)2\pi/a_0$ (see Methods section 'Imaging d-symmetry CDW $\widetilde{D}(\boldsymbol{q})$ and avoiding the CDW setup effect in $I_c(\boldsymbol{r})$'). Obviously, Fig. 4b and Fig. 4d are not identical, with the PDW exhibiting much narrower peaks and thus more spatial coherence. Nevertheless, this PDW wavevector (Fig. 4b, c) is not inconsistent (within joint error bars) with a conventionally defined wavevector of the cuprate CDW state at the same hole density[27]. However, the observed PDW also exhibits a primarily s/s'-symmetry form factor because Fig. 4b is based on the conventional sum over sublattices, while the CDW state exhibits a primarily d-symmetry form factor, as detected in the difference of sublattice-phase-resolved images[28] $\widetilde{O}_x(\boldsymbol{q}) - \widetilde{O}_y(\boldsymbol{q})$ (Fig. 4d).

The visualization of a Cooper-pair density wave, a long-term challenge in physics[1,2], has now been achieved using SJTM[22–24]. The subdominant PDW observed in $Bi_2Sr_2CaCu_2O_{8+x}$ at approximately the same wavevector as a CDW ($\boldsymbol{Q}_P \approx \boldsymbol{Q}_C$) and with s/s' form factor (Fig. 4), is consistent with Ginzburg–Landau theory[5,11,13,14] in the case

© 2016 Macmillan Publishers Limited. All rights reserved

(among others) where a *d*-symmetry superconductor coexists with a *d*-symmetry form factor CDW (see Methods section 'Analysing PDW within Ginzburg–Landau theory'). Microscopic theories for a cuprate PDW[5–9,13,16] requiring $\boldsymbol{Q}_P = \boldsymbol{Q}_C/2$ cannot be fully tested here because of the observed disorder in $\widetilde{I}_c(\boldsymbol{q})$ at low $\boldsymbol{q}$ (Fig. 4b). However, microscopic models for the pseudogap phase involving the interplay of *d*-symmetry Cooper pairing and a *d*-symmetry form factor CDW do yield a PDW with $\boldsymbol{Q}_P \approx \boldsymbol{Q}_C$ (refs 18–21) as in Fig. 4, although typically with a *d*-symmetry form factor. Moreover, the apparently lattice-commensurate value of $\boldsymbol{Q}_P$, which would arise naturally in strong-coupling theories for density modulations in a doped Mott insulator, motivates further study. Finally, our HTS-tip millikelvin-SJTM approach to nanometre-resolution Cooper-pair condensate imaging also reveals a direct route to visualization of FFLO[1,2] or PDW[6–21] states in other cuprates, iron pnictides and unconventional superconductors.

Online Content Methods, along with any additional Extended Data display items and Source Data, are available in the online version of the paper; references unique to these sections appear only in the online paper.

Received 18 November 2015; accepted 8 February 2016.
Published online 13 April 2016.

1. Fulde, P. & Ferrell, R. A. Superconductivity in a strong spin-exchange field. *Phys. Rev.* **135,** A550–A563 (1964).
2. Larkin, A. I. & Ovchinnikov, Y. N. Neodnorodnoe sostoyanie sverkhprovodnikov. *Zh. Eksp. Teor. Fis.* **47,** 1136–1146 (1964); Inhomogeneous state of superconductors. *Sov. Phys. JETP* **20,** 762–769 (1965).
3. Liao, Y. *et al.* Spin-imbalance in a one-dimensional Fermi gas. *Nature* **467,** 567–569 (2010).
4. Norman, M. R. & Pépin, C. The electronic nature of high temperature cuprate superconductors. *Rep. Prog. Phys.* **66,** 1547–1610 (2003).
5. Fradkin, E., Kivelson, S. A. & Tranquada, J. M. Theory of intertwined orders in high temperature superconductors. *Rev. Mod. Phys.* **87,** 457–482 (2015).
6. Himeda, A., Kato, T. & Ogata, M. Stripe states with spatially oscillating *d*-wave superconductivity in the two-dimensional *t*–*t*′–*J* model. *Phys. Rev. Lett.* **88,** 117001 (2002).
7. Raczkowski, M., Capello, M., Poilblanc, D., Frésard, R. & Oleś, A. M. Unidirectional *d*-wave superconducting domains in the two-dimensional *t*–*J* model. *Phys. Rev. B* **76,** 140505 (2007).
8. Yang, K.-Y., Chen, W. Q., Rice, T. M., Sigrist, M. & Zhang, F.-C. Nature of stripes in the generalized *t*–*J* model applied to the cuprate superconductors. *New J. Phys.* **11,** 055053 (2009).
9. Loder, F., Graser, S., Kampf, A. P. & Kopp, T. Mean-field pairing theory for the charge-stripe phase of high-temperature cuprate superconductors. *Phys. Rev. Lett.* **107,** 187001 (2011).
10. Corboz, P., Rice, T. M. & Troyer, M. Competing states in the *t*–*J* model: Uniform *d*-wave state versus stripe state. *Phys. Rev. Lett.* **113,** 046402 (2014).
11. Berg, E. *et al.* Dynamical layer decoupling in a stripe-ordered high-T_c superconductor. *Phys. Rev. Lett.* **99,** 127003 (2007).
12. Seo, K., Chen, H.-D. & Hu, J. Complementary pair-density-wave and *d*-wave-checkerboard orderings in high-temperature superconductors. *Phys. Rev. B* **78,** 094510 (2008).
13. Berg, E., Fradkin, E. & Kivelson, S. A. Charge-4*e* superconductivity from pair-density-wave order in certain high-temperature superconductors. *Nature Phys.* **5,** 830–833 (2009).
14. Agterberg, D. F. & Tsunetsugu, H. Dislocations and vortices in pair-density-wave superconductors. *Nature Phys.* **4,** 639–642 (2008).
15. Zelli, M., Kallin, C. & Berlinksy, A. J. Quantum oscillations in a π-striped superconductor. *Phys. Rev. B* **86,** 104507 (2012).
16. Lee, P. A. Amperean pairing and the pseudogap phase of cuprate superconductors. *Phys. Rev. X* **4,** 031017 (2014).
17. Chen, H.-D., Vafek, O., Yazdani, A. & Zhang, S.-C. Pair density wave in the pseudogap state of high temperature superconductors. *Phys. Rev. Lett.* **93,** 187002 (2004).
18. Pépin, C., de Carvalho, V. S., Kloss, T. & Montiel, X. Pseudogap, charge order, and pairing density wave at the hot spots in cuprate superconductors. *Phys. Rev. B* **90,** 195207 (2014).
19. Freire, H., de Carvalho, V. S. & Pépin, C. Renormalization group analysis of the pair-density-wave and charge order within the fermionic hot-spot model for cuprate superconductors. *Phys. Rev. B* **92,** 045132 (2015).
20. Wang, Y., Agterberg, D. F. & Chubukov, A. Interplay between pair- and charge-density-wave orders in underdoped cuprates. *Phys. Rev. B* **91,** 115103 (2015).
21. Wang, Y., Agterberg, D. F. & Chubukov, A. Coexistence of charge-density-wave and pair-density-wave orders in underdoped cuprates. *Phys. Rev. Lett.* **114,** 197001 (2015).
22. Naaman, O., Teizer, W. & Dynes, R. C. Fluctuation dominated Josephson tunneling with a scanning tunneling microscope. *Phys. Rev. Lett.* **87,** 097004 (2001).
23. Rodrigo, J. G., Suderow, H. & Vieira, S. On the use of STM superconducting tips at very low temperatures. *Eur. Phys. J. B* **40,** 483–488 (2004).
24. Proslier, Th. *et al.* Probing the superconducting condensate on a nanometer scale. *Europhys. Lett.* **73,** 962–968 (2006).
25. Nachumi, B. *et al.* Muon spin relaxation studies of Zn-substitution effects in high-T_c cuprate superconductors. *Phys. Rev. Lett.* **77,** 5421 (1996).
26. Slezak, J. A. *et al.* Imaging the impact on cuprate superconductivity of varying the interatomic distances within individual crystal unit cells. *Proc. Natl Acad. Sci. USA* **105,** 3203–3208 (2008).
27. Comin, R. & Damascelli, A. Resonant X-ray scattering studies of charge order in cuprates. *Ann. Rev. Cond. Matter Phys.* **7,** 369–405 (2016).
28. Fujita, K. *et al.* Direct phase-sensitive identification of a *d*-form factor density wave in underdoped cuprates. *Proc. Natl Acad. Sci. USA* **111,** E3026–E3032 (2014).
29. Comin, R. *et al.* Symmetry of charge order in cuprates. *Nature Mater.* **14,** 796–801 (2015).
30. Forgan, E. M. *et al.* The microscopic structure of charge density waves in underdoped $YBa_2Cu_3O_{6.54}$ revealed by X-ray diffraction. *Nature Comm.* **6,** 10064 (2015).

Acknowledgements We acknowledge and thank D. Agterberg, A. V. Balatsky, D. Chowdhury, A. Chubukov, E. Fradkin, R. Hulet, S. A. Kivelson, P. A. Lee, M. Norman, J. W. Orenstein, C. Pepin, S. Sachdev, J. Tranquada and Y. Wang for discussions and advice. The development and operation of HTS SJTM technology and M.H.H. and A.K. were funded by the Moore Foundation's EPiQS Initiative through grant number GBMF4544. S.D.E. acknowledges studentship funding from the EPSRC under grant number EP/G03673X/1. J.C.S.D. and A.P.M. acknowledge research support from the EPSRC through the grant programme 'Topological Protection and Non-Equilibrium States in Correlated Electron Systems'. S.U. and H.E. acknowledge support from a Grant-in-Aid for Scientific Research from the Ministry of Science and Education (Japan). S.H.J. and J.L. acknowledge support from the Institute for Basic Science, Korea under grant number IBS-R009-D1. J.C.S.D. and K.F. acknowledge salary support from the US Department of Energy, Office of Basic Energy Sciences, under contract number DEAC02-98CH10886. E.-A.K. acknowledges support from the US Department of Energy, Office of Basic Energy Sciences, Division of Materials Science and Engineering under award DE-SC0010313.

Author Contributions M.H.H., S.D.E., A.K., and J.L. developed the SJTM techniques and carried out the experiments. K.F., H.E. and S.U. synthesized and characterized the samples. M.H.H., S.D.E., A.K., S.H.J. and K.F. developed and carried out analyses. E.-A.K. and M.J.L. provided theoretical guidance. A.P.M., J.L. and J.C.S.D. supervised the project and wrote the paper with key contributions from M.H.H., S.D.E. and K.F. The manuscript reflects the contributions and ideas of all authors.

Author Information Reprints and permissions information is available at www.nature.com/reprints. The authors declare no competing financial interests. Readers are welcome to comment on the online version of the paper. Correspondence and requests for materials should be addressed to J.C.S.D. (jcseamusdavis@gmail.com) or J.L. (jinholee@snu.ac.kr).

© 2016 Macmillan Publishers Limited. All rights reserved

METHODS

Modelling phase diffusion Josephson dynamics for SJTM. The Josephson effect[31] is first described by

$$I = I_J \sin(\phi) \tag{3}$$

the relationship of the Cooper-pair current I through the junction to the phase difference ϕ between the two electrodes, with I_J the Josephson critical current. Second,

$$\frac{d\phi}{dt} = \frac{2e}{\hbar} V \tag{4}$$

relates the time evolution of that phase difference to the voltage across the junction. If the Josephson coupling energy $E_J = \frac{\hbar}{2e} I_J \gg kT$ so that effects of thermal fluctuations on ϕ can be ignored, there exists a steady-state solution to equations (3) and (4) where $V = 0$ for $I < I_J$. At 50 mK, the condition $E_J = kT$ corresponds to a Josephson critical current $I_J \approx 2$ nA.

Because of our operating junction resistance $R_N \approx 10\,M\Omega$, the maximum supercurrent used in the SJTM experiments described here was approximately 20 pA. Thus, our experimental junctions all lie in a regime where ϕ exhibits steady-state diffusion through the Josephson potential owing to thermal fluctuations[32–38]. This results in a voltage dropped across the junction while the Cooper-pair current is flowing. We analyse the Josephson $I(V)$ characteristics between our d-wave HTS tip and the $Bi_2Sr_2CaCu_2O_{8+x}$ (BSCCO) surface using this classic phase-diffusion model for small junctions[32,33] within which the $I(V)$ characteristic of the junction is given by

$$I(V_{JJ}) = \frac{1}{2} I_J^2 Z \frac{V_{JJ}}{V_{JJ}^2 + V_c^2} \tag{5}$$

V_{JJ} is the voltage across the junction and $V_c = \frac{2eZkT^*}{\hbar}$ with Z the impedance in series with the voltage source at the high frequencies relevant to repeated re-trapping of the diffusing phase. Importantly, $I(V_{JJ})$ is maximal at

$$I_c = \frac{\hbar}{8ekT^*} I_J^2 \tag{6}$$

where T^* is an effective temperature parameterizing how dissipative the phase evolution is. Spatially resolved measurements of $I_c(\boldsymbol{r})$ thus allow one to measure spatial modulations in $I_J^2(\boldsymbol{r})$ (refs 22–24).

Extended Data Fig. 1a shows a diagram of the hybrid spectroscopic-imaging STM/SJTM measurement circuit used. A load resistor $R_B = 10\,M\Omega$ is voltage-biased in series with the Josephson junction formed between the STM tip and the sample. Extended Data Fig. 1b shows the zero-frequency solutions to an electronic circuit model for this setup. The red and blue lines show the trajectories that the forwards and backwards sweeps take through the $I(V)$ plane. The nonlinearity of the circuit introduces discontinuities in the measured $I(V)$; a discontinuity occurs at the point where $I = I_c$ and thus makes this current experimentally identifiable by the sharp $I(V)$ feature associated with it. Extended Data Fig. 1c shows the same trajectories but as a function of the voltage across the junction V_{JJ}. This circuit's nonlinearity also generates hysteresis in the $I(V)$ characteristic even if the dynamics of the Josephson junction itself are over-damped at all frequencies. This hysteresis is indeed observed throughout our SJTM studies of BSCCO (Fig. 2d), and systematic errors due to the hysteresis are avoided during our $I_c(\boldsymbol{r})$ imaging experiments by sweeping the applied voltage always in the same direction once the Josephson junction has been formed at each location $\boldsymbol{r}$.

Characterizing $Bi_2Sr_2CaCu_2O_{8+x}$ nanoflake STM tips. To detect the gap modulations (equation (1)) requires single electron tunnelling from a non-superconducting electrode (NIS), while to observe the Josephson current modulations (equation (2)) requires Cooper-pair tunnelling from a superconducting electrode (SIS). For our SJTM studies, the high energy gap at the STM tip Δ_T is achieved by picking up a nanometre-sized flake of BSCCO onto the conventional tungsten microscope tip. Extended Data Fig. 1d shows the measured dI/dV spectrum of the tungsten tip before that process as a dashed line; it is precisely as expected for hole density $p \approx 17\%$ BSCCO samples. Simulation of the expected dI/dV for tunnelling between a BSCCO nanoflake tip and sample (solid line) is in good agreement with the typical SIS spectrum observed.

In Extended Data Fig. 2 we compare the performance of two completely different BSCCO nanoflake tips. Extended Data Fig. 2a and b shows their measured dI/dV spectra; they are obviously very similar. Extended Data Fig. 2c and d demonstrates the ~1-nm spatial resolution achieved in topographic images using these two tips. Extended Data Fig. 2e and f shows the Fourier transform of these two topographic images, demonstrating that the supermodulation is easily detected in both cases and that no other unusual characteristics, such as additional $\boldsymbol{q}$-space peaks or moiré patterns, are observed.

To check the relative orientation of the BSCCO nanoflake crystal axes to the axes of the sample, we evaluate simulations to see what might be expected of such a tip. Extended Data Fig. 3a and b shows a measured NIS topograph $T(\boldsymbol{r})$ of BSCCO taken with a conventional tungsten tip, and its Fourier transform. To simulate what would be observed if the crystal axes of a BSCCO nanoflake are oriented (or not) to those of the sample crystal axes we extract a typical ~2-nm-diameter patch from this image and then convolute the patch image with $T(\boldsymbol{r})$ at each location $\boldsymbol{r}$. This results in the simulated topograph that is expected when using a BSCCO nanoflake tip with (or without) axes aligned to the crystal axes. If the axes of the patch are aligned (Extended Data Fig. 3c) to the crystal, the result is as in Extended Data Fig. 3e (see the Fourier transform in the inset). If the axes are misaligned (Extended Data Fig. 3d) with the crystal the result is as in Extended Data Fig. 3f (see the Fourier transform in the inset). As the vivid moiré effects in the Fourier transform of the latter are not observed in the actual experiments (Extended Data Fig. 2e and f), we conclude that the axes of the nanoflake are aligned with those of the BSCCO bulk crystal.

Specifications for HTS-tip, millikelvin SJTM for condensate visualization. The technical challenge of large field-of-view nanometre-resolution SJTM imaging is to measure, in a reasonable time (days), an array of $I_c(\boldsymbol{r})$ values with ~1% precision using typically 256×256 pixels. Four basic elements are required: (1) an ultra-low-vibration dilution-refrigerator-based STM that is engineered for sub-picometre stability in taking spectroscopic data while out of feedback, and typically at $T = 50$ mK; (2) a high-temperature superconducting tip creation scheme which involves removing a nanometre-sized flake from the BSCCO surface and adhering it to the tip; (3) modification to the electronic circuitry to form a hybrid spectroscopic-imaging STM/SJTM operating condition (Fig. 2a) that allows conventional operation in the SIS configuration for topographic imaging and motion control, and bias voltage sweeps in the microvolt range when in Josephson mode; and (4) control of the capability to reliably and repeatedly carry out spectroscopic maps $I(V, \boldsymbol{r})$ using a junction resistance of ~10 MΩ at every $\boldsymbol{r}$ and with V spanning tens of microvolts.

Defining, measuring and imaging $I_c(\boldsymbol{r})$. Extended Data Fig. 4a shows the histogram of I_c values measured in a typical field of view during these studies. By averaging over the individual measured $I(V)$ from all the locations $\boldsymbol{r}$ contained within the bins indicated by the coloured arrows, we obtain the three representative Josephson $I(V)$ measurements shown in Extended Data Fig. 4b. They span the range of $I(V)$ characteristics measured at different locations. The coloured arrows in Extended Data Fig. 4b give examples where I_c is identified in a particular curve. In general we functionally define the quantity $I_c(\boldsymbol{r})$ reported in the main text to be the maximum magnitude of current achieved on sweeping away from $V = 0$. By comparison with Extended Data Fig. 1b, this current is the maximum Cooper-pair current, I_c, described by the phase diffusion model (see Methods section 'Modelling phase diffusion Josephson dynamics for SJTM') that at constant temperature and Z is directly proportional to $I_J^2(\boldsymbol{r})$.

Extended Data Fig. 5a, b and c shows typical examples of repeated $I_c(\boldsymbol{r})$ measurement experiments (with slightly different operating parameters but the same BSCCO nano-flake tip). The functionality and repeatability of this technique to achieve $I_c(\boldsymbol{r})$ imaging with nanometer resolution is clear.

The typical evolution of measured $I(V)$ during SJTM imaging of $I_c(\boldsymbol{r})$ at 45 mK at a specific sequence of locations (numbered 1–9 in Extended Data Fig. 5b) is shown in Extended Data Fig. 6. The almost complete (~95%) suppression of I_c as this sequence passes through the site of a Zn atom is seen in panel 5 of Extended Data Fig. 6. These typical data demonstrate directly the unprocessed signal-to-noise ratio for measurement of I_c and how spatial evolution of unprocessed $I(V)$ spectra yields the high fidelity seen in the $I_c(\boldsymbol{r})$ images.

In Extended Data Fig. 7a and b we show the topographic images taken with the same BSCCO nanoflake tip before and after a typical $I_c(\boldsymbol{r})$ mapping experiment. Comparison of the topographs shows them to be virtually identical and demonstrates that no significant changes occur in the geometry of the tip during the map. The implication is that the nanoflake at the end of the tip never once touches the surface, and that all such $I_c(\boldsymbol{r})$ studies reported are in the true SIS tunnelling limit and are very far from making any point contact.

Finally, our model is that the BSCCO tip has maximum gap Δ_T and negligible modulating component, while that of the sample Δ_S has two components Δ_S^0 (background component) and Δ_S^P (PDW component) and $\Delta_S = \Delta_S^0 + \Delta_S^P$ with $\Delta_S^0 \gg \Delta_S^P$. The Josephson coupling then consists of a primary coupling that occurs between the uniform components, and a secondary coupling that is between the uniform component of the tip and the modulated component of the sample (as in equation (2)) with the empirical result of convolution presented in Fig. 4. To leading order $I_c(\boldsymbol{r})$ is then linear in the PDW component of both the sample gap and superfluid density.

Visualizing supermodulation-induced PDW and $R_N(\boldsymbol{r})$. In principle, SJTM allows direct measurement of modulations in the superconducting order

© 2016 Macmillan Publishers Limited. All rights reserved

parameter amplitude through the product $I_J R_N$. Here, I_J is the intrinsic, $T=0$, Josephson critical current of the junction and R_N is a characteristic resistance of the single-particle tunnelling channel. In taking this product, variations that affect the matrix elements for tunnelling of Cooper pairs and the single-particle tunnelling conductance ($1/R_N$) in the same way cancel out.

We use dI/dV at a bias voltage V_B far higher than the SIS gap edge as an estimate of the ungapped, 'normal state' junction conductance G_N. Simultaneous measurement of this value and $I_c(\boldsymbol{r})$ were not possible because the former requires V_B in tens of millivolts while the latter requires V_B of a few tens of microvolts. Moreover, in the picometre range tip–sample separations used in measuring $I_c(\boldsymbol{r})$, the single-particle tunnelling current can become destructively large to our BSCCO nanoflake tip. Thus the following procedure was adopted:

(1) Measure $I_c(\boldsymbol{r})$ with setpoint current $I_s = I_{s1}$ and bias voltage $V_s = V_{s1}$, as shown in Extended Data Fig. 8a.

(2) In the same field of view measure $g_1(\boldsymbol{r}, E)$, defined as dI/dV for bias voltages V_{s1} to $-V_{s1}$ with setpoint condition $I_s = I_{s1}$, $V_s = V_{s1}$.

(3) In the same field of view measure $g_2(\boldsymbol{r}, E)$ defined as dI/dV with setpoint condition $I_s = I_{s2}$, $V_s = V_{s2}$ for bias voltages V_{s2} to $-V_{s2}$, where $V_{s2} \gg V_{s1}$ and $V_{s2} > \Delta_{SIS}$.

(4) Over the range $V = [-V_{s1}, V_{s1}]$ determine the coefficients $\alpha(\boldsymbol{r})$ and $\beta(\boldsymbol{r})$, which scale $g_2(\boldsymbol{r})$ onto $g_1(\boldsymbol{r})$ via $g_1(\boldsymbol{r}, E) = \alpha(\boldsymbol{r}) g_2(\boldsymbol{r}, E) + \beta(\boldsymbol{r})$. In doing the scaling a small region of voltages near $V=0$ where the Cooper-pair tunnelling (Josephson) signal exhibits is excluded.

(5) $R_N(\boldsymbol{r})$ for junctions used to measure $I_c(\boldsymbol{r})$ is then determined by $1/R_N(\boldsymbol{r}) = G_N(\boldsymbol{r}) = \alpha(\boldsymbol{r})/2(g_2(\boldsymbol{r}, +V_{s2}) + g_2(\boldsymbol{r}, -V_{s2})) + \beta(\boldsymbol{r})$, as shown in Extended Data Fig. 8b.

Now we consider the case of the cuprate supermodulation PDW where the bulk quasi-periodic distortion of the $Bi_2Sr_2CaCu_2O_{8+x}$ crystal at wavevector $\boldsymbol{Q}_{SM}$ leads to modulations of the measured $I_c(\boldsymbol{r})$ at the same wavevector superposed on the larger background.

$$\begin{aligned}\Delta(\boldsymbol{r}) \propto I_J(\boldsymbol{r}) R_N(\boldsymbol{r}) &= (I_J^0 + I_J^P \cos(\boldsymbol{Q}_{SM}\cdot\boldsymbol{r}))(R_N^0 + R_N^P \cos(\boldsymbol{Q}_{SM}\cdot\boldsymbol{r} + \varphi)) \\ &= I_J^0 R_N^0 + R_N^0 I_J^P \cos(\boldsymbol{Q}_{SM}\cdot\boldsymbol{r}) + I_J^0 R_N^P \cos(\boldsymbol{Q}_{SM}\cdot\boldsymbol{r} + \varphi) + \cdots \end{aligned} \quad (7)$$

where we allow for an arbitrary phase difference φ between modulation in I_J and R_N at $\boldsymbol{Q}_{SM}$. For any value of φ, one may neglect the third term if

$$I_J^0 R_N^P \ll R_N^0 I_J^P \Leftrightarrow \frac{R_N^P}{R_N^0} \div \frac{I_J^P}{I_J^0} \ll 1 \quad (8)$$

In the experiments presented in the main text we measure the quantity

$$I_c(\boldsymbol{r}) \propto (I_J^0)^2 + 2 I_J^0 I_J^P \cos(\boldsymbol{Q}_{SM}\cdot\boldsymbol{r}) + \cdots \quad (9)$$

as shown in Extended Data Fig. 8a. In Extended Data Fig. 8b we show $R_N(\boldsymbol{r})$ derived as above. By comparing the amplitude of $\widetilde{I}_c(\boldsymbol{q})$ and $\widetilde{R}_N(\boldsymbol{q})$ at $\boldsymbol{q} = \boldsymbol{Q}_{SM}$ normalized to their $\boldsymbol{q} = \boldsymbol{0}$ value one may directly determine $\frac{R_N^P}{R_N^0} \div \frac{I_J^P}{I_J^0}$ as in Extended Data Fig. 9c; we find that this ratio is far less than 1 and hence modulations in $\Delta(\boldsymbol{r})$ at $\boldsymbol{Q}_{SM}$ are faithfully represented by those measured in $I_c(\boldsymbol{r})$.

Inset to Extended Data Fig. 8c is $|\widetilde{R}_N(\boldsymbol{q})|$, showing directly that variations in the $\widetilde{R}_N(\boldsymbol{q})$ near $\boldsymbol{q} \approx (0.25, 0)2\pi/a_0$ and equivalent are negligible, so that measurement of $I_c(\boldsymbol{r})$ should and does yield a faithful image of the condensate.

Imaging *d*-symmetry CDW $\widetilde{D}(\boldsymbol{q})$ and avoiding the CDW setup effect in $I_c(\boldsymbol{r})$. The *d*-symmetry form factor density wave in underdoped cuprates (refs 39–41) has been directly detected by spectroscopic-imaging STM by analysing the differential conductance $dI/dV \equiv g(\boldsymbol{r}, V)$ images in terms of $\widetilde{D}(\boldsymbol{q}) = \widetilde{O}_x(\boldsymbol{q}) - \widetilde{O}_y(\boldsymbol{q})$ which extracts the *d*-symmetry form factor density wave signature at the correct wavevector. At dopings near optimal, it is known from several experimental techniques that the intensity of the *d*-symmetry form factor density wave diminishes rapidly[42]. Therefore, to improve the visualization of the *d*-symmetry form factor density wave signature at such high dopings as used here, we use topographic information instead. In constant-current topographic imaging, the STM feedback system adjusts the tip–sample separation, T, as it scans over the sample surface to maintain a setpoint current, I_s, at a constant applied tip–sample bias V_s. The topographic image $T(\boldsymbol{r})$ is related to the tunnelling current

$$I(\boldsymbol{r}, T, V) = f(\boldsymbol{r}, T) \int_0^{eV_s} \mathrm{LDOS}(\boldsymbol{r}, \epsilon) \mathrm{d}\epsilon \quad (10)$$

and assuming that the function $f(\boldsymbol{r}, T)$, which represents the effect of corrugation, work function, and tunnelling matrix elements, takes the form

$$f(\boldsymbol{r}, T) = \exp(-\kappa T) A(\boldsymbol{r}) \quad (11)$$

where κ is the tunnel-barrier-height factor and depends on the work functions of the sample and tip, and LDOS is the local density of electronic states. The recorded value of the relative tip–sample separation is then

$$T(\boldsymbol{r}) = \frac{1}{\kappa} \ln\left[\int_0^{eV_s} \mathrm{LDOS}(\boldsymbol{r}, \epsilon) \mathrm{d}\epsilon\right] + \frac{1}{\kappa} \ln\left[\frac{I_s}{A(\boldsymbol{r})}\right] \quad (12)$$

Thus high signal-to-noise topographic images obtained by constant-current STM imaging reveal contributions from both the surface structure and variations in the LDOS($\boldsymbol{r}, E$).

While a single cuprate topographic image will contain the signature of the *d*-symmetry form factor density wave, subtracting one topographic image from another taken at opposite bias polarity can further enhance the cuprate CDW signal. This is because the cuprate *d*-symmetry form factor density wave modulates in anti-phase[41] between empty and filled states and hence a subtraction of topographic images measured near the pseudogap energy ($|V_s| \approx 100$ meV in equation (12)) formed with biases $+V_s$ and $-V_s$ should amplify the CDW contrast.

In Extended Data Fig. 9a and b we demonstrate this procedure using two high-resolution, high-signal-to-noise ratio topographs $T(\boldsymbol{r})$ taken at opposite bias polarities (100 mV and −100 mV) with the same conventional tungsten tip; they are spatially registered to each other with picometre precision[40]. Extended Data Fig. 9c is the difference of these topographs, from which the two oxygen-sublattice-sampled images $O_x(\boldsymbol{r})$; $O_y(\boldsymbol{r})$ are then extracted, and $\widetilde{D}(\boldsymbol{q}) = \widetilde{O}_x(\boldsymbol{q}) - \widetilde{O}_y(\boldsymbol{q})$ calculated. An image of $\widetilde{D}(\boldsymbol{q})$ reveals a primarily *d*-symmetry form factor density wave because of the existence of four maxima at the CDW wavevector $\boldsymbol{Q}_C = (\pm 0.22, 0)2\pi/a_0$ and $(0, \pm 0.22)2\pi/a_0$ as in Fig. 4d (refs 39 and 41).

One important implication of the fact that the topographic/CDW modulations have *d*-symmetry form factor is for avoidance of the setup effect when measuring $I_c(\boldsymbol{r})$. Equation (12) shows that $T(\boldsymbol{r})$ is affected logarithmically by the term $\int_0^{eV_s} \mathrm{LDOS}(\boldsymbol{r}, \epsilon) \mathrm{d}\epsilon$. This means the tip–surface distance will be modulated at the same $\boldsymbol{Q}$ as modulations in LDOS($\boldsymbol{r}, \epsilon$). One concern might be that, because the CDW modulations produce $T(\boldsymbol{r})$ (that is, the tip–sample distance) modulations at this $\boldsymbol{Q}$, this will generate a spurious $I_c(\boldsymbol{r})$ modulation at the identical $\boldsymbol{Q}$. This would be the infamous 'setup effect', but now affecting SJTM.

However, because the CDW in cuprates has a predominant *d*-symmetry form factor, any conventional image $T(\boldsymbol{r})$ and its Fourier transform $\widetilde{T}(\boldsymbol{q})$ that are formed by adding the three sublattice images exhibit the actual modulations at wavevector $\boldsymbol{Q} = \boldsymbol{Q}_{Bragg} \pm \boldsymbol{Q}_C = (1 \pm 0.22, 0)2\pi/a_0$ and $(0, 1 \pm 0.22)2\pi/a_0$. These only become detectable at the correct CDW wavevector $\boldsymbol{Q}_C$ when one uses a measure of *d*-symmetry form factor: $\widetilde{D}(\boldsymbol{q}) = \widetilde{O}_x(\boldsymbol{q}) - \widetilde{O}_y(\boldsymbol{q})$. Therefore CDW modulations in the unprocessed topograph $T(\boldsymbol{r})$; $\widetilde{T}(\boldsymbol{q})$ occur at $\boldsymbol{Q} \approx (0.78, 0)2\pi/a_0$ and $(0, 0.78)2\pi/a_0$ (dashed red circles in the Extended Data Fig. 10a). Because they are at a completely different wavevector, it is impossible for such modulations to produce, through a setup effect, spurious $I_c(\boldsymbol{r})$ modulations at $\boldsymbol{Q} \approx (0.25, 0)2\pi/a_0$ and $(0, 0.25)2\pi/a_0$. Therefore the PDW wavevector $\boldsymbol{Q}_P$ observed directly by SJTM, and shown in the Extended Data Fig. 10b and in Fig. 4b, is not generated spuriously by a systematic setup effect due to the coexisting CDW.

Analysing PDW within Ginzburg–Landau theory. PDW modulations may be induced by the coupling between a translationally invariant superconducting order parameter and a CDW. We focus on the case of a tetragonal system with $\boldsymbol{q} = \boldsymbol{0}$ superconducting order of B_{1g} ($d_{x^2-y^2}$) symmetry, a CDW order parameter with a purely *d*-symmetry form factor[43] and an induced secondary PDW order parameter with *s*/*s*′ symmetry form factor. The pairing amplitude is expanded in terms of superconducting order parameters via

$$\begin{aligned}\phi(\boldsymbol{r}, \boldsymbol{r}') \equiv \psi_\sigma(\boldsymbol{r})\psi_{-\sigma}(\boldsymbol{r}') &= D(\boldsymbol{r} - \boldsymbol{r}')\Delta_0(\boldsymbol{R}) \\ &+ S'(\boldsymbol{r} - \boldsymbol{r}')\{\Delta_{\boldsymbol{Q}}(\boldsymbol{R})e^{i\boldsymbol{Q}\cdot\boldsymbol{R}} + \Delta_{-\boldsymbol{Q}}(\boldsymbol{R})e^{-i\boldsymbol{Q}\cdot\boldsymbol{R}} + \Delta_{\overline{\boldsymbol{Q}}}(\boldsymbol{R})e^{i\overline{\boldsymbol{Q}}\cdot\boldsymbol{R}} + \Delta_{-\overline{\boldsymbol{Q}}}(\boldsymbol{R})e^{-i\overline{\boldsymbol{Q}}\cdot\boldsymbol{R}}\} \end{aligned} \quad (13)$$

where $\boldsymbol{R} = (\boldsymbol{r} - \boldsymbol{r}')/2$, $D(\boldsymbol{r} - \boldsymbol{r}')$ and $S'(\boldsymbol{r} - \boldsymbol{r}')$ are the *d*- and *s*′-form factors that either do or do not change sign under 90° rotations. This expansion then defines five complex order parameters that enter the free energy: Δ_0, $\Delta_{\boldsymbol{Q}}$, $\Delta_{-\boldsymbol{Q}}$, $\Delta_{\overline{\boldsymbol{Q}}}$ and $\Delta_{-\overline{\boldsymbol{Q}}}$. $\Delta_{\boldsymbol{Q}}$ and $\Delta_{-\boldsymbol{Q}}$ are required to be independent to implement the U(1) spatial phase degree of freedom because $\phi(\boldsymbol{r}, \boldsymbol{r}')$ itself is complex. $\boldsymbol{Q}$ and $\overline{\boldsymbol{Q}}$ are along symmetry-equivalent orthogonal directions. Under a 90° rotation the B_{1g} superconducting and *s*/*s*′ form factor PDW order parameters transform as $\Delta_0 \rightarrow -\Delta_0$ and $\Delta_{\boldsymbol{Q}} \rightarrow \Delta_{\overline{\boldsymbol{Q}}}, \Delta_{\overline{\boldsymbol{Q}}} \rightarrow \Delta_{-\boldsymbol{Q}}, \Delta_{-\boldsymbol{Q}} \rightarrow \Delta_{-\overline{\boldsymbol{Q}}}, \Delta_{-\overline{\boldsymbol{Q}}} \rightarrow \Delta_{\boldsymbol{Q}}$.

In a similar way, the CDW order parameter is

$$\begin{aligned}\phi_c(\boldsymbol{r}, \boldsymbol{r}') &\equiv \langle \psi_\sigma^\dagger(\boldsymbol{r})\psi_\sigma(\boldsymbol{r}') + \psi_\sigma^\dagger(\boldsymbol{r}')\psi_\sigma(\boldsymbol{r})\rangle \\ &= D(\boldsymbol{r} - \boldsymbol{r}')\{\psi_{\boldsymbol{Q}}(\boldsymbol{R})e^{i\boldsymbol{Q}\cdot\boldsymbol{R}} + \psi_{-\boldsymbol{Q}}(\boldsymbol{R})e^{-i\boldsymbol{Q}\cdot\boldsymbol{R}} + \psi_{\overline{\boldsymbol{Q}}}(\boldsymbol{R})e^{i\overline{\boldsymbol{Q}}\cdot\boldsymbol{R}} + \psi_{-\overline{\boldsymbol{Q}}}(\boldsymbol{R})e^{-i\overline{\boldsymbol{Q}}\cdot\boldsymbol{R}}\} \\ &\{\psi_{\boldsymbol{Q}}(\boldsymbol{R})e^{i\boldsymbol{Q}\cdot\boldsymbol{R}} + \psi_{-\boldsymbol{Q}}(\boldsymbol{R})e^{-i\boldsymbol{Q}\cdot\boldsymbol{R}} + \psi_{\overline{\boldsymbol{Q}}}(\boldsymbol{R})e^{i\overline{\boldsymbol{Q}}\cdot\boldsymbol{R}} + \psi_{-\overline{\boldsymbol{Q}}}(\boldsymbol{R})e^{-i\overline{\boldsymbol{Q}}\cdot\boldsymbol{R}}\} \end{aligned} \quad (14)$$

© 2016 Macmillan Publishers Limited. All rights reserved

This will contribute two independent complex order parameters to the free energy expansion. Since the CDW order parameter must be real $\psi_{-\boldsymbol{Q}} = \psi^*_{\boldsymbol{Q}}$. For purely d-symmetry form factor CDW, the order parameter will have the following property under a 90° rotation: $\psi_{\boldsymbol{Q}} \rightarrow -\psi_{\overline{\boldsymbol{Q}}}$, $\psi_{\overline{\boldsymbol{Q}}} \rightarrow -\psi_{-\boldsymbol{Q}}$, $\psi_{-\boldsymbol{Q}} \rightarrow -\psi_{-\overline{\boldsymbol{Q}}}$, $\psi_{-\overline{\boldsymbol{Q}}} \rightarrow -\psi_{\boldsymbol{Q}}$. Now consider the symmetry-allowed free energy terms that will couple Δ_0, the Δ_Q values and the $\psi_{\boldsymbol{Q}}$ values. The leading term is simply:

$$\gamma_1[\Delta_0^*\{\psi_{\boldsymbol{Q}}\Delta_{-\boldsymbol{Q}} + \psi_{-\boldsymbol{Q}}\Delta_{\boldsymbol{Q}} + \psi_{\overline{\boldsymbol{Q}}}\Delta_{-\overline{\boldsymbol{Q}}} + \psi_{-\overline{\boldsymbol{Q}}}\Delta_{\overline{\boldsymbol{Q}}}\} + c \cdot c] \quad (15)$$

Because the PDW order parameters appear to the power of unity in this term, the free energy can always be lowered by making $\Delta_{\boldsymbol{Q}}$ non-zero, if both Δ_0^* and $\psi_{\overline{\boldsymbol{Q}}}$ are non-zero. Thus the co-existence of $d_{x^2-y^2}$ superconductivity and a d-symmetry form factor CDW at wave-vector $\boldsymbol{Q}$ will induce a PDW at wavevector $\boldsymbol{Q}$ with an s/s' symmetry form factor.

We note that such a coupling is not unique. There exists a similar symmetry-allowed term in the free energy admitting a d-symmetry form factor PDW where the $\Delta_{\boldsymbol{Q}}$ values now transform under 90 degree rotation, like the $\psi_{\boldsymbol{Q}}$ values. The associated free energy term will have a relative negative sign between the first two terms and the second two terms of equation (15). As the experimentally detected PDW has s/s' form factor we do not discuss this further here.

Code availability. The data files for the results presented here and the codes used in their analysis are available at http://dx.doi.org/10.17630/83957a84-2186-4c14-8e55-f961a19ec9a9.

31. Josephson, B. D. Possible new effects in superconductive tunneling. *Phys. Lett.* **1,** 251–253 (1962).
32. Ambegaokar, V. & Halperin, B. I. Voltage due to thermal noise in the dc Josephson effect. *Phys. Rev. Lett.* **22,** 1364–1366 (1969); erratum **23,** 274 (1969).
33. Ivanchenko, Y. M. & Zil'berman, L. A. The Josephson effect in small tunnel contacts. *Sov. Phys. JETP* **28,** 1272–1276 (1969).
34. Devoret, M. H. *et al.* Effect of the electromagnetic environment on the Coulomb blockade in ultrasmall tunnel junctions. *Phys. Rev. Lett.* **64,** 1824–1827 (1990).
35. Falci, G., Bubanja, V. & Schön, G. Quantum tunnelling in small-capacitance Josephson junctions in a general electromagnetic environment. *Europhys. Lett.* **16,** 109–114 (1991).
36. Martinis, J. M. & Kautz, R. L. Classical phase diffusion in small hysteretic Josephson junctions. *Phys. Rev. Lett.* **63,** 1507–1510 (1989).
37. Iansiti, M., Tinkham, M., Johnson, A. T., Smith, W. F. & Lobb, C. J. Charging effects and quantum properties of small superconducting tunnel junctions. *Phys. Rev. B* **39,** 6465 (1989).
38. Šmakov, J., Martin, I. & Balatsky, A. V. Josephson scanning tunneling microscopy. *Phys. Rev. B* **64,** 212506 (2001).
39. Fujita, K. *et al.* Spectroscopic imaging scanning tunneling microscopy studies of electronic structure in the superconducting and pseudogap phases of cuprate high-T_c superconductors. *J. Phys. Soc. Jpn.* **81,** 011005 (2012).
40. Hamidian, M. H. *et al.* Picometer registration of zinc impurity states in $Bi_2Sr_2CaCu_2O_{8+\delta}$ for phase determination in intra-unit-cell Fourier transform STM. *New J. Phys.* **14,** 053017 (2012).
41. Hamidian, M. H. *et al.* Atomic-scale electronic structure of the cuprate *d*-symmetry form factor density wave state. *Nature Phys.* **12,** 150–156 (2016).
42. Fujita, K. *et al.* Simultaneous transitions in cuprate momentum-space topology and electronic symmetry breaking. *Science* **344,** 612–616 (2014).
43. Sachdev, S. & La Placa, R. Bond order in two-dimensional metals with anti-ferromagnetic exchange interactions. *Phys. Rev. Lett.* **111,** 027202 (2013).

© 2016 Macmillan Publishers Limited. All rights reserved

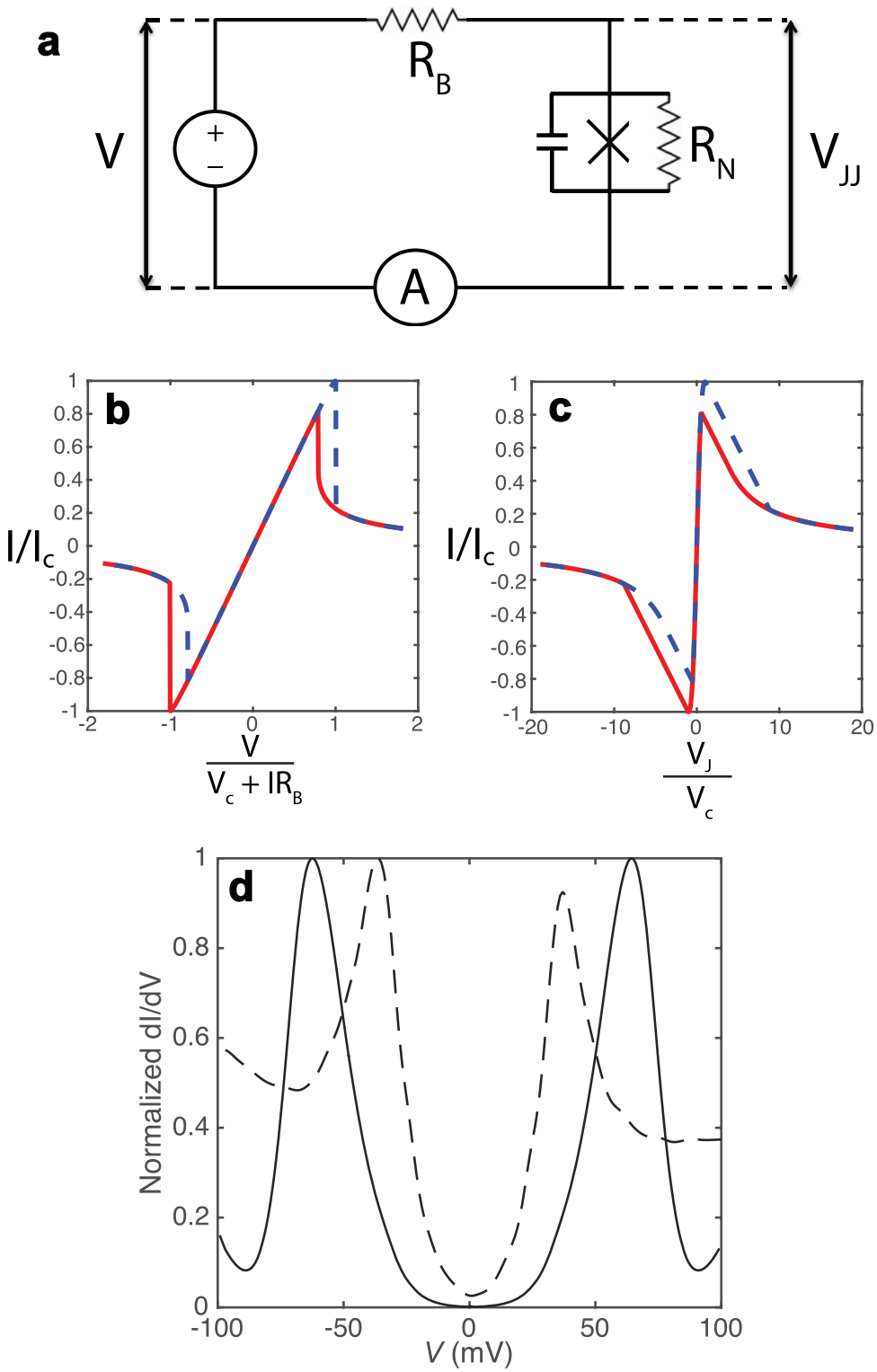

Extended Data Figure 1 | SJTM circuit model and phase diffusion dynamics. a, Circuit diagram of the hybrid spectroscopic-imaging STM/SJTM setup used in these experiments. The voltage source V is from the usual STM bias controller; the load resistor $R_B = 10\,M\Omega$; the single-particle tunnelling resistance of the Josephson junction formed between the tip and sample is R_N, and the voltage actually developed across the junction is V_{JJ}. **b**, The dynamics of this circuit produces two predominant effects. First there is a sudden change in the $I(V)$ characteristic measured with the external ammeter shown, when the current reaches a value $I_c = \frac{\hbar}{8ekT^*} I_J^2$ where I_J is the zero-temperature Josephson critical current and T^* is an effective temperature parameterizing the dissipative environment of the junction. The second predicted effect is strong hysteresis depending on which direction the external voltage is swept; this is shown as the difference between the solid-red and dashed-blue lines. Both effects are seen very clearly and universally in the measured $I(V)$ throughout our studies reported here. **c**, The relationship of the current as in **b** but in terms of the voltage across the Josephson junction V_{JJ}. **d**, The dashed curve represents a typical dI/dV spectrum on as-grown BSCCO sample, measured using a normal metallic tungsten tip. The solid line is a simulation for an expected dI/dV spectrum when using a BSCCO superconducting tip; we use the standard equation for tunnelling between two superconductors, each with the density of states identical to the dashed line. The result, in very good agreement with the typical measured SIS spectrum, is shown in Fig. 2b.

© 2016 Macmillan Publishers Limited. All rights reserved

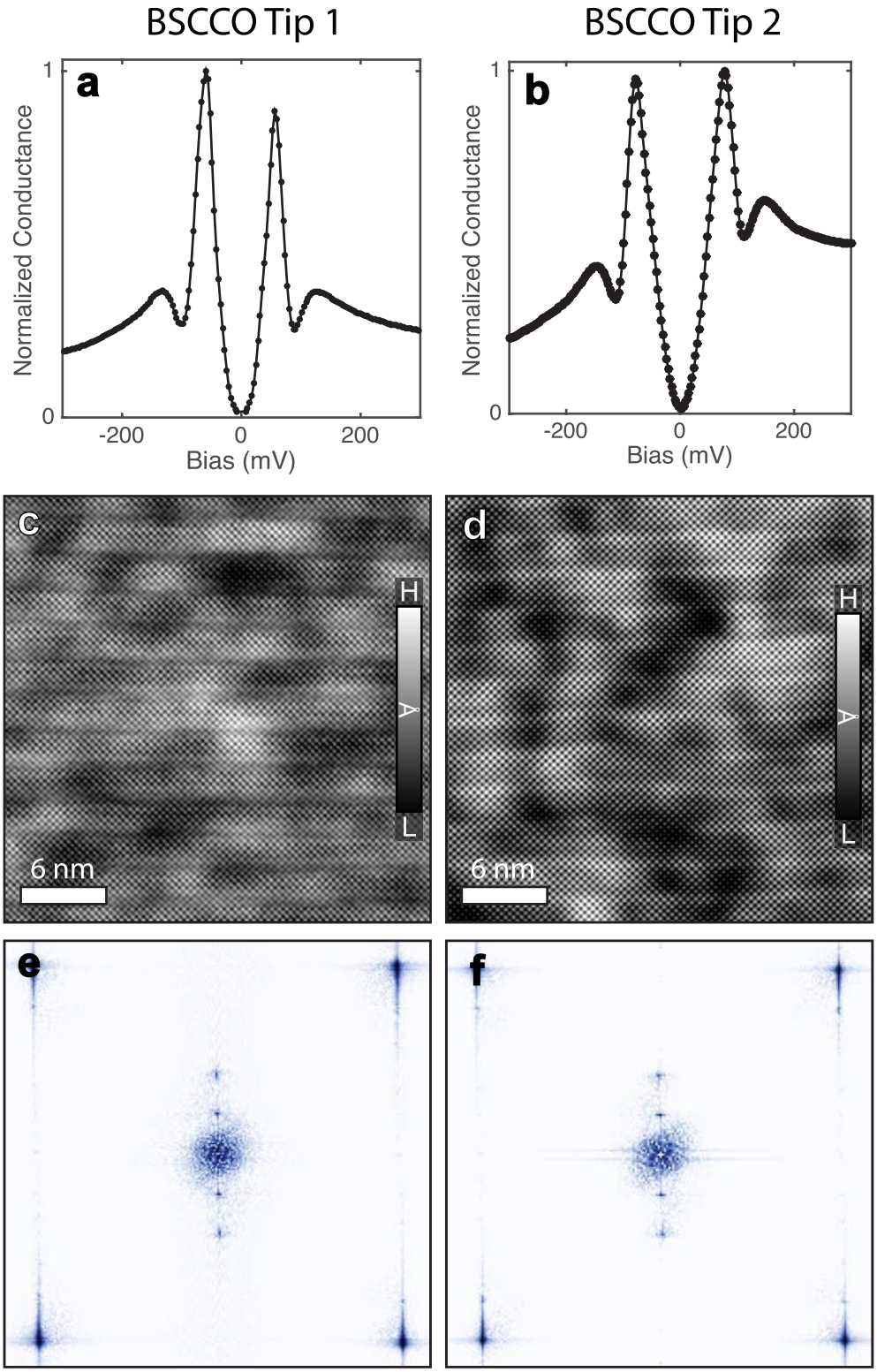

Extended Data Figure 2 | Spectroscopic/topographic data from two distinct BSCCO tips. Typical dI/dV spectrum, topography and magnitude of its Fourier transform $\widetilde{T}(\boldsymbol{q})$ measured with two completely distinct BSCCO tips on two different BSCCO samples: tip 1 (**a**, **c** and **e**) and tip 2 (**b**, **d** and **f**).

© 2016 Macmillan Publishers Limited. All rights reserved

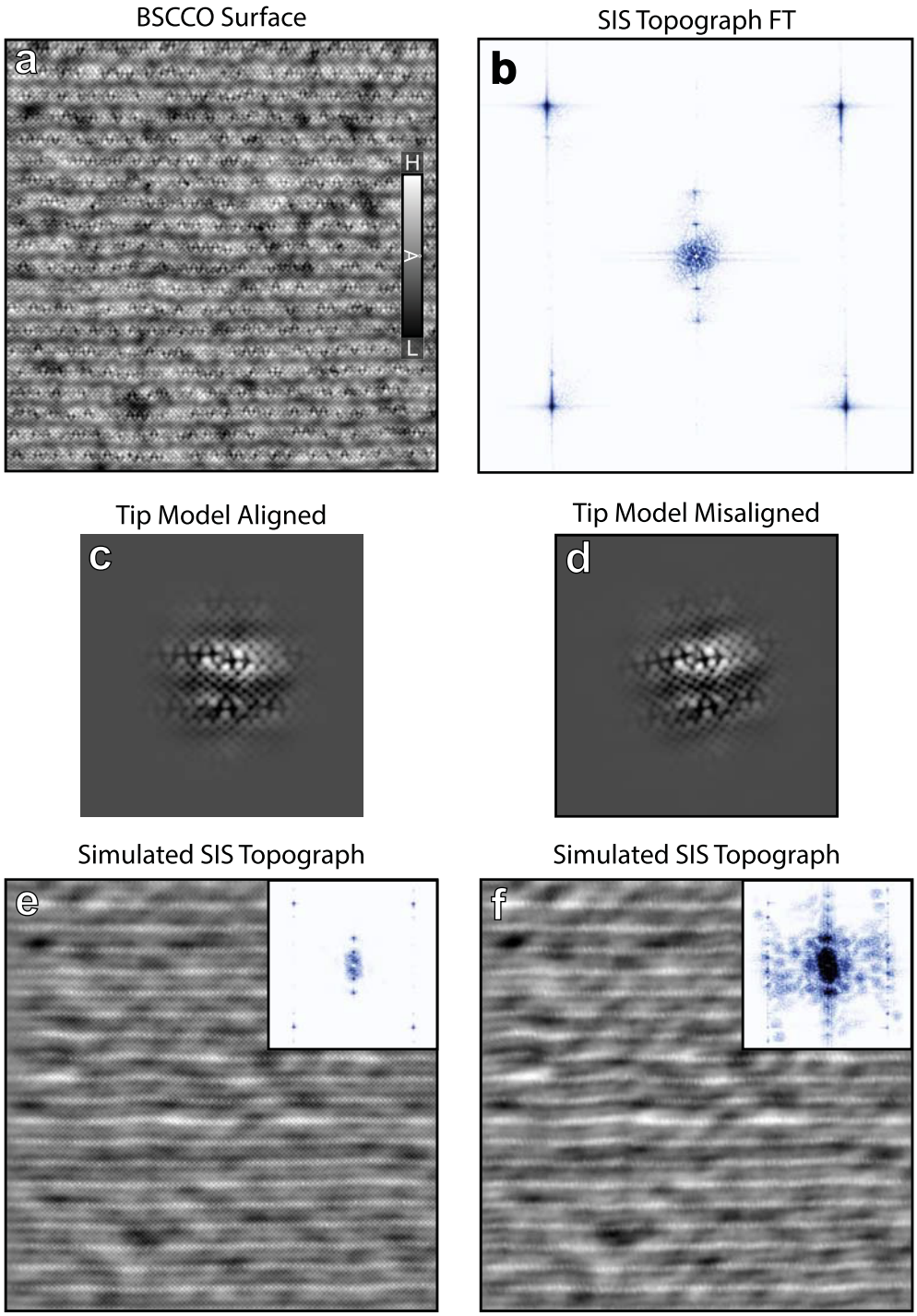

Extended Data Figure 3 | Simulation of topography with BSCCO nanoflake tip. a, Surface topography $T(\boldsymbol{r})$ of BSCCO sample; image obtained with a conventional metallic tungsten tip. **b**, Magnitude of Fourier transform (FT) of **a**. **c**, Model for BSCCO nanoflake tip that is aligned with the BSCCO surface in **a**. **d**, Model for BSCCO nanoflake tip that is misaligned with the BSCCO surface in **a**. **e**, Convolution of BSCCO surface image in **a** and aligned BSCCO nanoflake tip in **c**. Inset shows resultant Fourier Transform with Bragg peaks in the corners and supermodulation peaks. **f**, Convolution of BSCCO surface image in a and misaligned BSCCO nanoflake tip in **d**. Inset shows resulting Fourier transform with many additional broad peaks caused by moiré pattern effects. Comparison to **e** demonstrates that the tip used in the studies reported here was well aligned with the sample.

© 2016 Macmillan Publishers Limited. All rights reserved

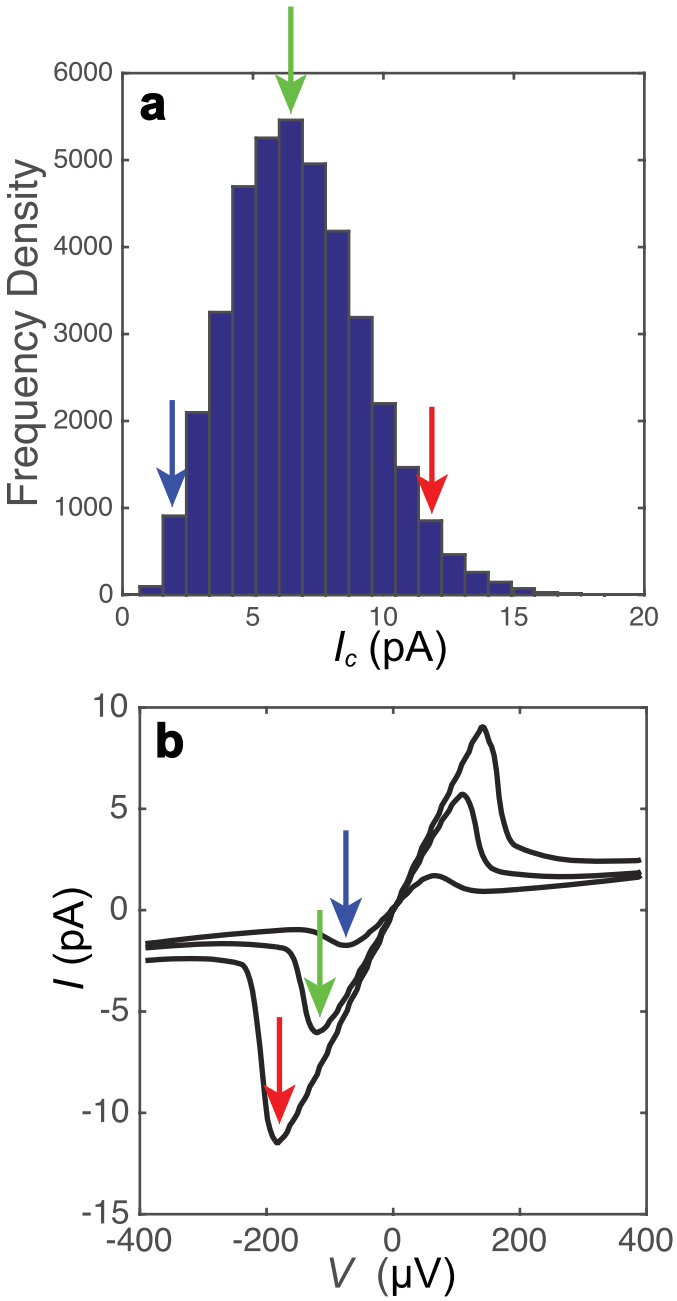

Extended Data Figure 4 | Spatial variation of HTS tip–sample Josephson junction *I*(*V*). a, A histogram of all I_c values measured at different locations in the field of view shown in Fig. 3b. The characteristic I_c values associated with the three spectra in **b** are indicated by the coloured arrows. **b**, Three $I(V)$ formed by averaging the constituent $I(V)$ from the bins indicated by the coloured arrows in **a**. They demonstrate the variation in the measured $I(V)$ characteristic that occurs at different locations in the field of view shown in Fig. 3b. The three I_c values are indicated by coloured arrows.

© 2016 Macmillan Publishers Limited. All rights reserved

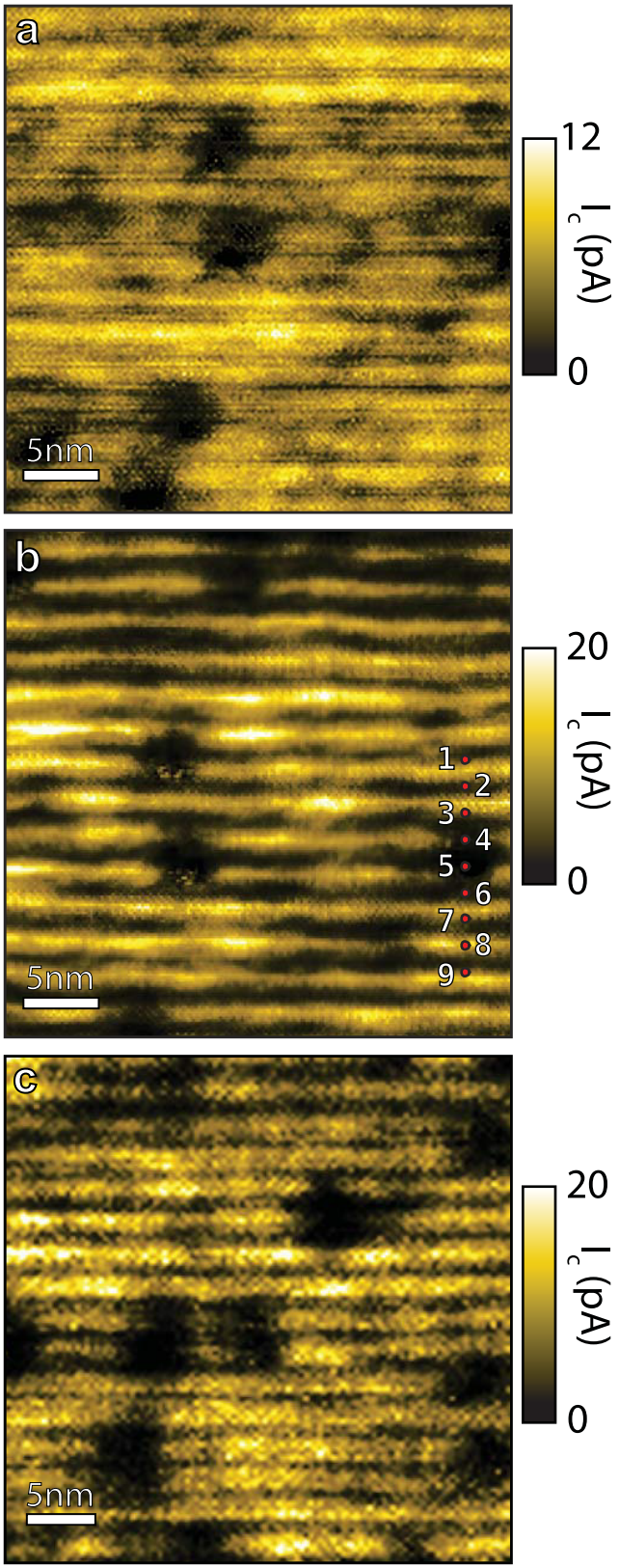

Extended Data Figure 5 | Repeatable utility of BSCCO nanoflake tips for $I_c(r)$ mapping. Three $I_c(r)$ images **a**, **b** and **c** measured with the same BSCCO nanoflake tip, at different times (separated by many days) and using different Josephson junction parameters, but closely related in fields of view. Repeatability and fidelity of our $I_c(r)$ imaging by SJTM is evident.

© 2016 Macmillan Publishers Limited. All rights reserved

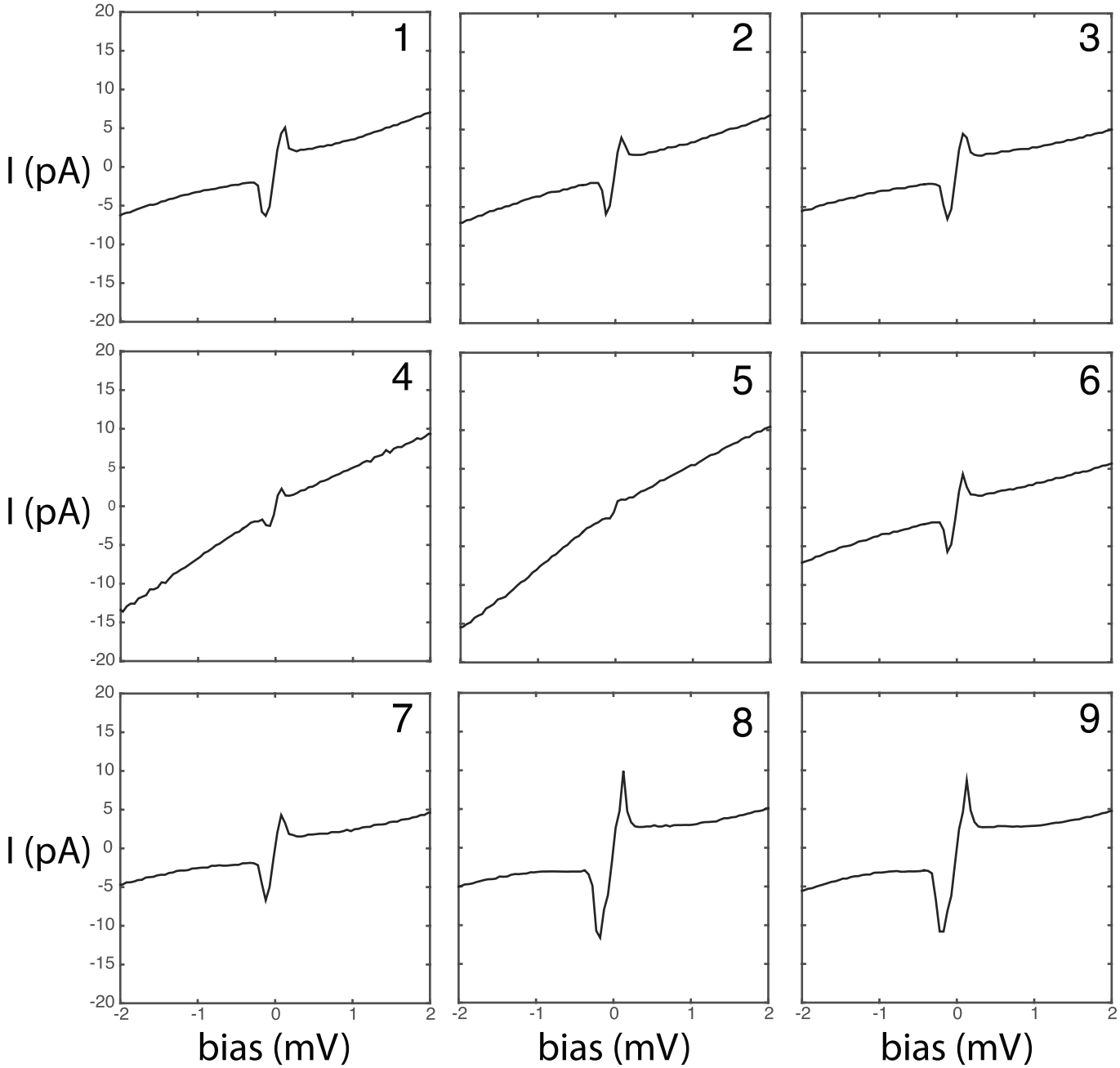

Extended Data Figure 6 | Sequence of measured $I_c(r)$ along line in Extended Data Fig. 5b. Nine individual $I(V)$ spectra measured at the locations indicated by numbers 1–9 in Extended Data Fig. 5b. In each case the transition from the SIS resistive branch to the phase diffusion Josephson tunnelling branch is evident. Moreover, as the sequence passes through the site of a Zn atom, the value of I_c diminishes by ~95% from its maximum, as expected from muon spin rotation experiments. Bias, V_B.

© 2016 Macmillan Publishers Limited. All rights reserved

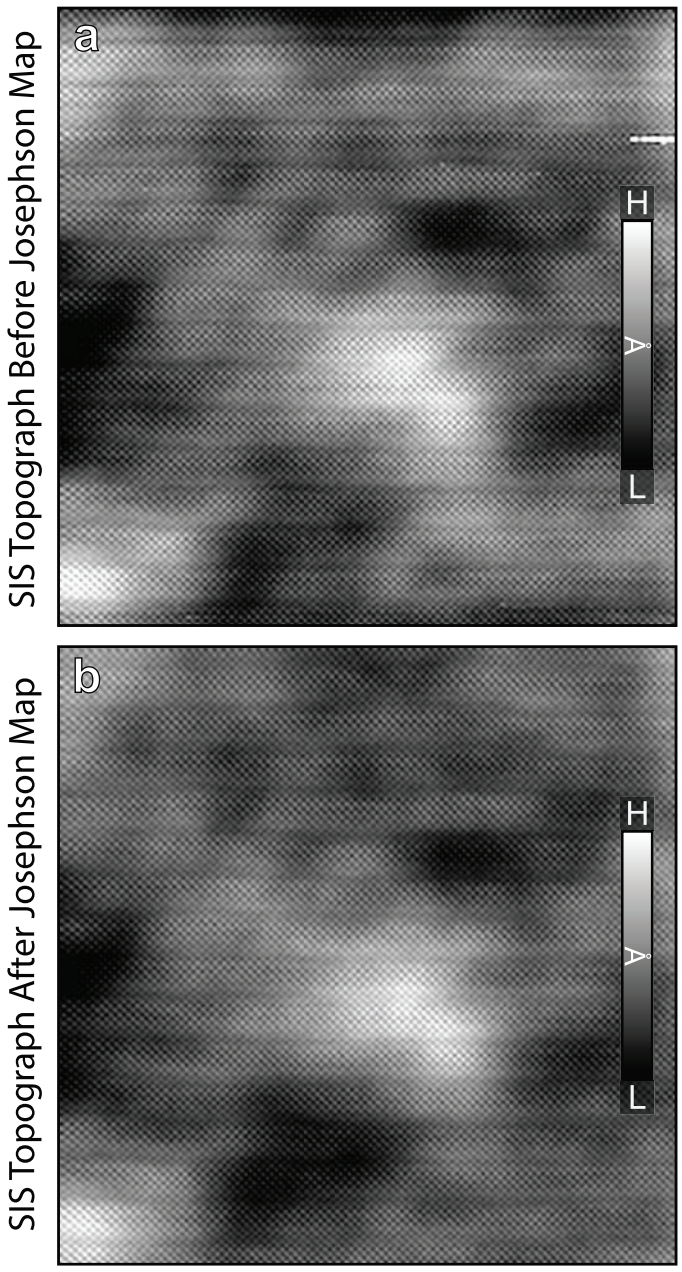

Extended Data Figure 7 | Before and after topographic images bracketing $I_c(r)$ map. a, Topograph taken with BSCCO tip before typical $I_c(r)$ SJTM map. **b**, Topograph taken with same BSCCO tip after the same $I_c(r)$ SJTM map as **a**. Comparison of **a** and **b** shows that tip and surface are very well preserved in our SJTM protocol.

© 2016 Macmillan Publishers Limited. All rights reserved

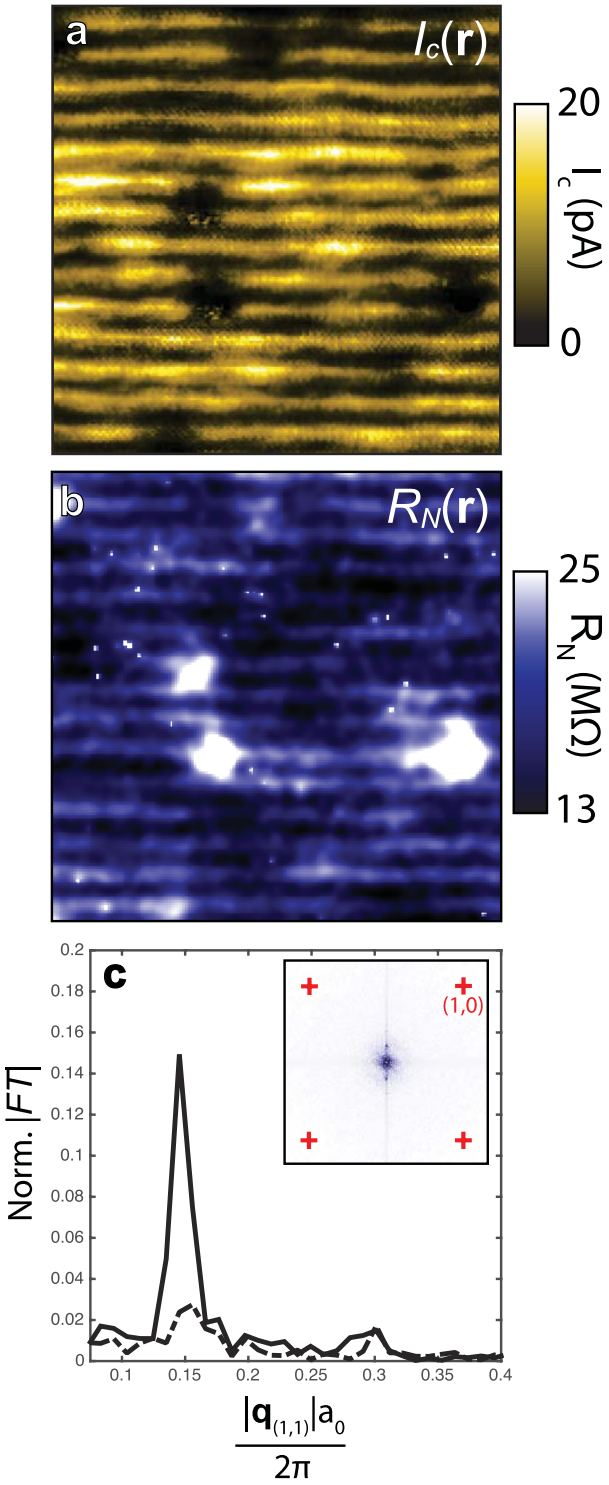

Extended Data Figure 8 | Comparison of modulations in $I_c(r)$ and $R_N(r)$. **a**, A typical measured $I_c(r)$ image of $Bi_2Sr_2CaCu_2O_{8+x}$ with the crystal supermodulation effect retained and apparent as strong spatial modulations in I_c along the vertical axis. **b**, Measured $R_N(r)$ image simultaneous with **a**, with the crystal supermodulation effect retained. The spatial modulations in $R_N(r)$ along the vertical axis are greatly diminished in relative amplitude compared to $I_c(r)$ modulations in **a**. **c**, Inset shows $|\widetilde{R}_N(q)|$, the magnitude of the Fourier transform of $R_N(r)$ from **b**. Plotting the simultaneously measured Fourier amplitudes of $\widetilde{I}_c(q)$ and $\widetilde{R}_N(q)$ along the (1, 1) direction passing through the wavevector of the supermodulation Q_{SM} shows that modulations in $\widetilde{R}_N(q)$ are negligible. Therefore the predominant effect in the $I_c(r)R_N(r)$ studied through this work is caused by the $I_c(r)$ variations, coming from the superfluid density variations $\rho_S(r) \propto I_J^2(r) \propto I_c(r)$of the condensate in the sample.

© 2016 Macmillan Publishers Limited. All rights reserved

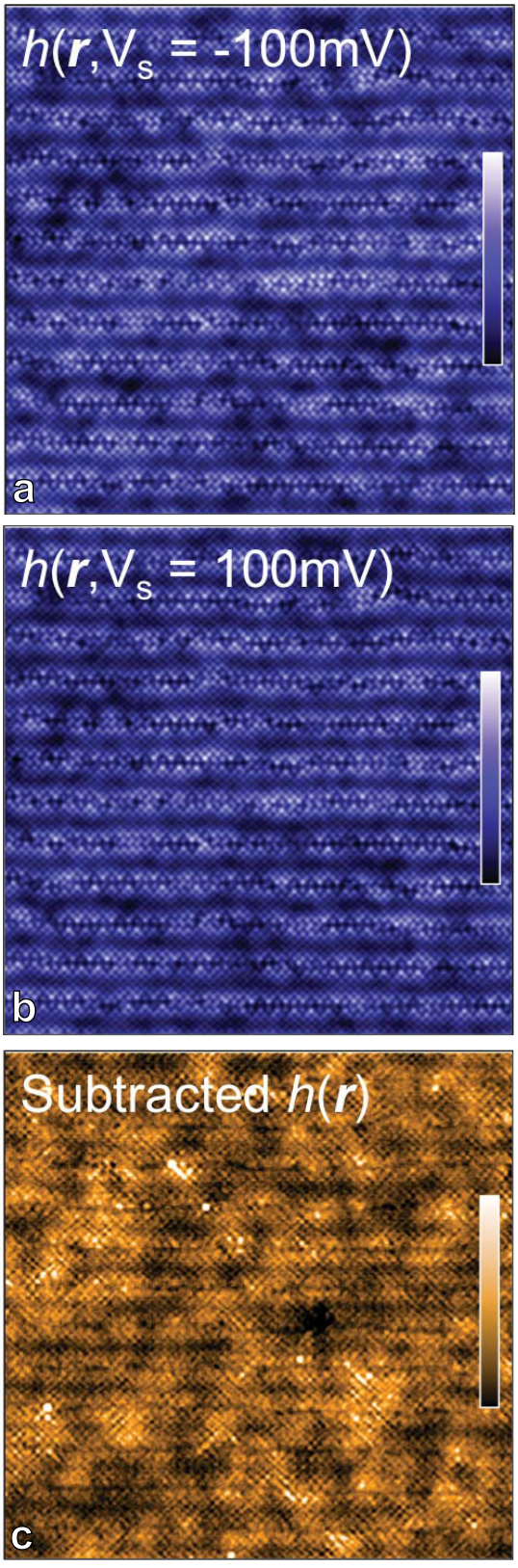

Extended Data Figure 9 | *d*-symmetry density wave $\widetilde{D}(\boldsymbol{q})$ from topography. a, High-resolution topographic image of typical BiO surface at the same hole-density as the $I_c(\boldsymbol{r})$ studies, measured at $V = 100$ meV. **b**, High-resolution topographic image of identical (registered for every atom within about 10 picometres) BiO surface as a measured at $V = -100$ meV. **c**, Difference between **a** and **b**; a CDW exhibits its signature logarithmically in such an image and therefore it can be used to detect the *d*-symmetry form factor density wave, as in Fig. 4d of the main text.

© 2016 Macmillan Publishers Limited. All rights reserved

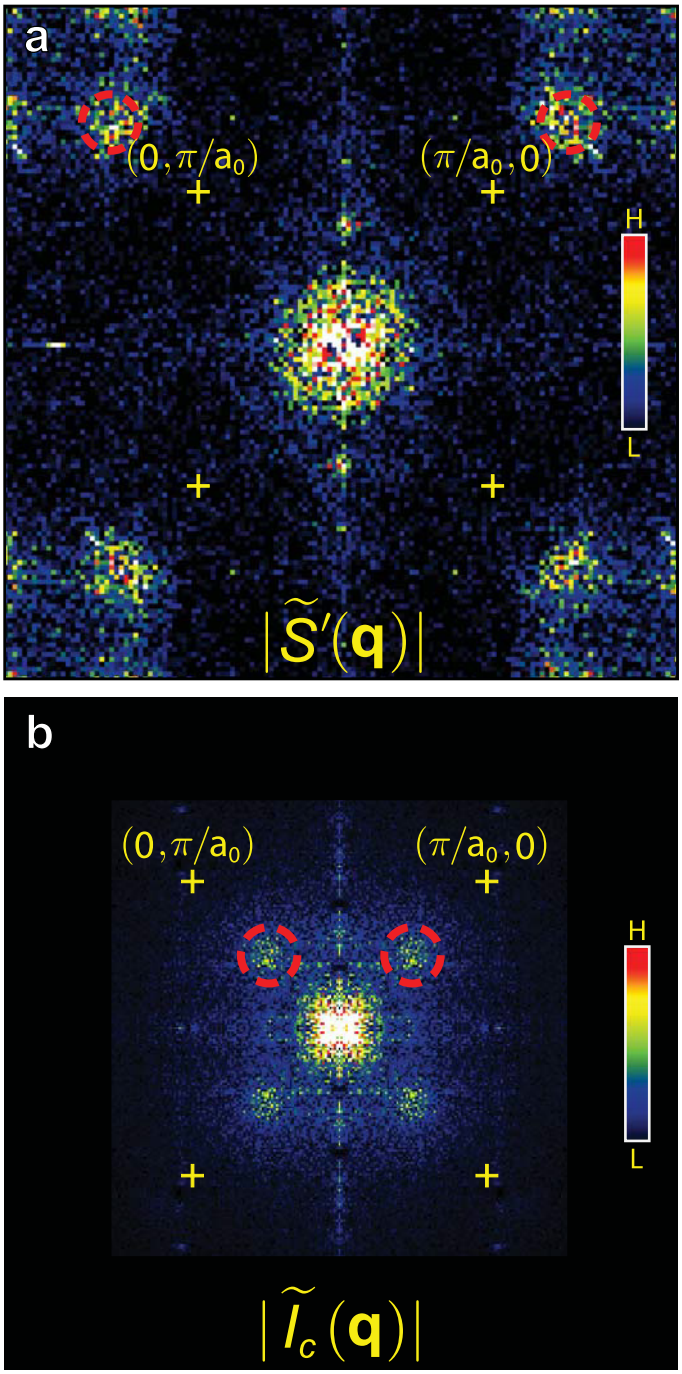

Extended Data Figure 10 | Absence CDW setup effect in $I_c(r)$. **a**, $\widetilde{T}(\boldsymbol{q})$, the Fourier transform magnitude of the sublattice-resolved image $O_x(\boldsymbol{r}) + O_y(\boldsymbol{r})$ derived from $\delta T(\boldsymbol{r})$, the difference between the two unprocessed topographic images $T(\boldsymbol{r}, \pm 100\,\text{meV})$ in Extended Data Fig. 9. We see directly that the actual modulations in topography due to the density of states modulations from the CDW occur at wavevectors $(1 \pm 0.22, 0)2\pi/a_0$ and $(0, 1 \pm 0.22)2\pi/a_0$ (dashed circles), as has been reported extensively in the past. These only become detectable at the actual CDW wavevector $\boldsymbol{Q}_C = (0.22, 0)2\pi/a_0$ and $(0, 0.22)2\pi/a_0$ when one uses a measure of *d*-symmetry form factor modulations: $\widetilde{D}(\boldsymbol{q}) = \widetilde{O}_x(\boldsymbol{q}) - \widetilde{O}_y(\boldsymbol{q})$, as shown in Fig. 4d. Because the physically real modulations in topography and conductance imaging therefore occur at $\boldsymbol{Q} = (0.78, 0)2\pi/a_0$ and $(0, 0.78)2\pi/a_0$ (dashed circles), it is impossible for them to produce, through a 'setup effect', spurious $I_c(\boldsymbol{r})$ modulations at the PDW wavevector $\boldsymbol{Q}_P \approx (0.25, 0)2\pi/a_0$ and $(0, 0.25)2\pi/a_0$, as indicated by dashed circles in **b**. **b**, The measured $\boldsymbol{q}$-space structure $\widetilde{I}_c(\boldsymbol{q})$ (which samples all sublattices in the conventional form $\widetilde{O}_x(\boldsymbol{q}) + \widetilde{O}_y(\boldsymbol{q}) + \widetilde{C}u(\boldsymbol{q})$. The PDW maxima occur at $\boldsymbol{Q}_P \approx (0.25, 0)2\pi/a_0$ and $(0, 0.25)2\pi/a_0$.

© 2016 Macmillan Publishers Limited. All rights reserved